Computational study of the collapse of a cloud with 12 500 gas bubbles in a liquid

U. Rasthofer, F. Wermelinger, P. Karnakov, J. Šukys, and P. Koumoutsakos*
Computational Science and Engineering Laboratory, ETH Zurich, Clausiusstr. 33, 8092 Zurich, Switzerland

(Received 29 April 2018; published 7 June 2019)

We investigate the collapse of a cloud composed of 12 500 gas bubbles in a liquid through large-scale simulations. The gas bubbles are discretized by a diffuse interface method, and a finite volume scheme is used to solve on a structured Cartesian grid the Euler equations. We investigate the propagation of the collapse wave front through the cloud and provide comparisons to existing models such as Mørch's ordinary differential equations and a homogeneous mixture approach. We analyze the flow field to examine the evolution of individual gas bubbles and in particular their associated microjet. We find that the velocity magnitude of the microjets depends on the local strength of the collapse wave and hence on the radial position of the bubbles in the cloud. At the same time, the direction of the microjets is influenced by the distribution of the bubbles in its vicinity. We envision that the present, state-of-the-art, large-scale simulations will serve the further development of low-order models for bubble collapse.

DOI: 10.1103/PhysRevFluids.4.063602

I. INTRODUCTION

Collapsing and interacting bubbles are encountered in a variety of industrial and scientific applications ranging from cavitation phenomena associated with engineering devices, such as marine propellers, hydroelectric turbines, and fuel injectors [1–3], to noninvasive biomedical procedures, for instance, kidney stone lithotripsy, drug delivery, and tissue ablation histotripsy [4–6]. The collective (growth and) rapid collapse of a large number of bubbles, i.e., a cloud of bubbles, in a liquid subjected to large pressure variation has been investigated both experimentally and numerically. Experiments in Ref. [7] studied the collapse of a cloud of bubbles via the formation of an inward propagating shock wave and the geometric focusing of this shock at the center of the cloud. Experimental measurements with hydrofoils subjected to cloud cavitation, conducted in Ref. [8], showed that very large pressure pulses occur within the cloud and are radiated outward during the collapse process. A technique developed in Ref. [9] allowed for controlling the bubble distance within a two-dimensional cloud. The study revealed the shielding effect of the outer bubbles and showed the formation of an inward-directed microjet. The final stage of the collapse of a hemispherical cloud near a solid surface was investigated using ultra-high-speed photography in Ref. [10]. Cloud cavitation in a water jet was examined in Ref. [11]. Various numerical studies were also reported in the literature; for instance, early ones assuming a potential flow in the liquid in Refs. [12,13]. The recently presented study [14] used an Euler-Lagrange approach, combining the Navier-Stokes equations with subgrid-scale spherical bubbles governed by a Rayleigh-Plesset-like equation, to investigate spherical clouds collapsing near a rigid wall. A similar approach was applied in Ref. [15] to study the impulsive loads generated by a cloud with 400 bubbles under an imposed

*petros@ethz.ch

oscillating pressure field. Resolved and deforming bubbles were considered in Refs. [16–19]. A two-dimensional simulation of the collapse of a small cluster with seven bubbles in an incompressible liquid using a front-tracking method was presented in Ref. [16]. The collapse dynamics of a cloud composed of 125 vapor bubbles with random radii was studied in Ref. [17], while Ref. [18] reported the evolution of a hemispherical cloud of 50 air bubbles. In Ref. [18] a homogeneous mixture model and a coupled system of Rayleigh-Plesset-like equations were considered in addition, but provided qualitatively different predictions of the pressure field. A recent study [19] addressed uncertainty quantification for the collapse of clouds with 500 randomly located gas bubbles. The goal of the present paper is to advance the state of the art in studies of cloud collapse processes by simulating thousands of gas bubbles and studying their collective interactions.

Numerical methods for multicomponent flow that resolve both components on the computational grid may be classified into single-fluid and two-fluid approaches. In two-fluid methods, each component is governed by an individual set of conservation equations for mass, momentum and energy, and discontinuities at the interface are treated explicitly [20–23]. In contrast, single-fluid methods, such as the diffuse interface method [24–27], introduce a zone around each interface where the transition from one component to the other is smeared over a few grid cells. In this context, single-fluid models present a compromise between accuracy and computational efficiency; that is, both components are explicitly distinguished, while the same numerical scheme can be used throughout the computational domain. This feature renders diffuse interface methods particularly appropriate for the large-scale simulation of flow problems with thousands of bubbles, as demonstrated by the compressible multicomponent flow solver presented in Ref. [28] which showed a throughput of up to 7×10^{11} computational cells per second on 96 racks of the IBM Sequoia.

Here we employ an extended version of this compressible multicomponent flow solver to simulate the collapse process of a cloud of 12 500 resolved gas bubbles. The number of bubbles in the present simulation is up to two orders of magnitude larger than the ones considered in previous studies. Clouds of this size recover the separation of scales, i.e., a cloud of large extent formed by small bubbles. Therefore, the present cloud complies with the assumptions of Mørch's ordinary differential equation for the propagation of the pressure wave resulting from the cloud collapse. At the same time, the large bubble count enables reliable statistics on the behavior of the individual bubbles and their associated microjets.

The paper is organized as follows: Sec. II summarizes the governing equations together with the computational method and presents the setup of the cloud collapse problem. Section III reports on the cloud collapse dynamics from a macroscopic point of view. In Sec. IV the dynamical behavior of the bubbles and their associated microjets is analyzed. Section V concludes the study.

II. GOVERNING EQUATIONS AND COMPUTATIONAL APPROACH

In the following, we summarize the governing equations, the applied numerical scheme, and the setup of the cloud collapse problem. The simulation presented in this study is conducted using the open source software Cubism-MPCF [28–30] for download. The reader is referred to Ref. [31] for the verification and validation of the compressible multicomponent flow solver for two-component shock-tube problems and for single-bubble collapse. Additionally, a grid convergence study for a small spherical cloud composed of 400 air bubbles is shown in Appendix A.

A. Governing equations

We study the collapse process of a cloud of gas (i.e., air) bubbles in a liquid (i.e., water). The two components, water and air, are assumed immiscible and are captured by the diffuse interface method for compressible multicomponent flows. The present investigation involves the collapse of highly nonspherical bubbles that come along with strong microjets. In the case of strong microjets, inertia forces dominate the initial stages of the collapse process, while viscous effects and surface

tension may be considered negligible; see Refs. [18,32]. This assumption is justified in Appendix A for a major part of the precollapse phase of the cloud, i.e., the time period before the cloud reaches the state of minimum gas volume. However, during the final stages of the bubble collapse, when the bubble scales are small and local interface curvatures are high, surface tension and viscosity may influence some details of the bubble collapse process. Being aware of these limitations of our approach, we exclude data corresponding to this collapse phase from our microscopic analyses.

Hence, we adopt the Euler equations consisting of the mass conservation equations for each component, conservation equations for momentum and total energy in mixture- (or single-) fluid formulation, and a transport equation for the volume fraction of one of the two components:

$$\frac{\partial \alpha_1 \rho_1}{\partial t} + \nabla \cdot (\alpha_1 \rho_1 \mathbf{u}) = 0, \tag{1}$$

$$\frac{\partial \alpha_2 \rho_2}{\partial t} + \nabla \cdot (\alpha_2 \rho_2 \mathbf{u}) = 0, \tag{2}$$

$$\frac{\partial (\rho \mathbf{u})}{\partial t} + \nabla \cdot (\rho \mathbf{u} \otimes \mathbf{u} + p\mathbf{I}) = \mathbf{0}, \tag{3}$$

$$\frac{\partial E}{\partial t} + \nabla \cdot [(E + p)\mathbf{u}] = 0, \tag{4}$$

$$\frac{\partial \alpha_2}{\partial t} + \mathbf{u} \cdot \nabla \alpha_2 = K \nabla \cdot \mathbf{u}, \tag{5}$$

where

$$K = \frac{\alpha_1 \alpha_2 \left(\rho_1 c_1^2 - \rho_2 c_2^2\right)}{\alpha_1 \rho_2 c_2^2 + \alpha_2 \rho_1 c_1^2}; \tag{6}$$

see Refs. [33,34] for derivation. In Eqs. (1)–(5), $\mathbf{u}$ denotes the velocity, p the pressure, $\mathbf{I}$ the identity tensor, ρ the (mixture) density, and E the (mixture) total energy $E = \rho e + 1/2\rho(\mathbf{u} \cdot \mathbf{u})$, where e is the (mixture) specific internal energy. Moreover, ρ_k, α_k, and c_k with $k \in \{1, 2\}$ are density, volume fraction, and speed of sound of the two components, respectively. It holds that $\alpha_1 + \alpha_2 = 1$ as well as $\rho = \alpha_1 \rho_1 + \alpha_2 \rho_2$ and $\rho e = \alpha_1 \rho_1 e_1 + \alpha_2 \rho_2 e_2$ for the mixture quantities. The source term on the right-hand side of the transport equation for α_2 was originally derived in Ref. [35] and is nonzero within the diffuse interface only. It allows for treating the interface zone as a compressible, homogeneous mixture of gas and liquid by capturing the reduction of the gas volume fraction when a compression wave travels across the mixing region and the increase for an expansion wave. As shown in Refs. [27,31], the inclusion of this term notably increases the accuracy and lowers the resolution requirements. Moreover, it allows for a smooth transition to a homogeneous mixture model, if the resolution limit is reached by a collapsed bubble.

The system of Eqs. (1)–(5) is closed by the stiffened equation of state [36]:

$$p = (\gamma_k - 1)\rho_k e_k - \gamma_k p_{c,k}, \tag{7}$$

where isobaric closure is assumed [34]. The speed of sound is then given by

$$\rho_k c_k^2 = \gamma_k (p + p_{c,k}). \tag{8}$$

The material parameters γ_k and $p_{c,k}$ are assumed constant. Here the values of Refs. [18,25] are used, which are given by $\gamma_1 = 4.4$ and $p_{c,1} = 6.0 \times 10^2$ MPa for water and $\gamma_2 = 1.4$ and $p_{c,2} = 0.0$ MPa for air.

B. Numerical method

The system of governing equations (1)–(5) is expressed in a quasiconservative form as

$$\frac{\partial \mathbf{Q}}{\partial t} + \nabla \cdot \mathbf{F} = \mathbf{R}, \tag{9}$$

where $\mathbf{Q} = (\alpha_1\rho_1, \alpha_2\rho_2, \rho\mathbf{u}, E, \alpha_2)^{\mathrm{T}}$. The vector $\mathbf{F} = (\mathbf{F}^{(x)}, \mathbf{F}^{(y)}, \mathbf{F}^{(z)})^{\mathrm{T}}$ combines the fluxes $\mathbf{F}^{(x)} = (\alpha_1\rho_1 u_x, \alpha_2\rho_2 u_x, \rho u_x^2 + p, \rho u_y u_x, \rho u_z u_x, (E+p)u_x, \alpha_2 u_x)^{\mathrm{T}}$, $\mathbf{F}^{(y)} = (\alpha_1\rho_1 u_y, \alpha_2\rho_2 u_y, \rho u_x u_y, \rho u_y^2 + p, \rho u_z u_y, (E+p)u_y, \alpha_2 u_y)^{\mathrm{T}}$, and $\mathbf{F}^{(z)} = (\alpha_1\rho_1 u_z, \alpha_2\rho_2 u_z, \rho u_x u_z, \rho u_y u_z, \rho u_z^2 + p, (E+p)u_z, \alpha_2 u_z)^{\mathrm{T}}$. The right-hand-side vector $\mathbf{R} = (0, 0, 0, 0, 0, 0, [K + \alpha_2]\,\nabla \cdot \mathbf{u})^{\mathrm{T}}$ is zero except for the last component, which comprises the source term of Eq. (5) and a contribution obtained from reformulating its convective term.

We solve Eq. (9) using a Godunov-type finite volume method on a uniform Cartesian grid. The choice of a uniform Cartesian grid enables the exploitation of High Performance Computing (HPC) architectures [28]. The numerical fluxes at the cell faces are computed by an HLLC approximate Riemann solver, originally introduced for single-phase flow in Ref. [37] and more recently extended to multicomponent flows in Refs. [27,38,39]. The fluxes are based on the primitive variables $\mathbf{u}$, p, $\alpha_1\rho_1$, $\alpha_2\rho_2$, and α_2 at the cell faces, which are reconstructed from the cell average values using a shock-capturing third-order WENO scheme [40]. Primitive variables are used for reconstruction to prevent numerical instabilities at the interface [38,41]. The approach suggested in Ref. [38] is adopted for the application of the HLLC Riemann solver to the evolution of α_2. In summary, the resulting semidiscrete system reads as

$$\frac{d\mathbf{V}(t)}{dt} = \mathcal{L}[\mathbf{V}(t)], \tag{10}$$

where $\mathbf{V}$ denotes the vector of cell average values and $\mathcal{L}(\cdot)$ the spatially discrete forms of divergence and source term in Eq. (9). Equation (10) is discretized in time by a total variation diminishing (TVD), low-storage, explicit third-order Runge-Kutta scheme [42] with a time step dictated by the Courant-Friedrichs-Lewy (CFL) condition.

C. Cloud setup

We investigate an initially spherical cloud of radius $R_{\mathrm{C}} = 45$ mm, composed of $n_{\mathrm{B}} = 12\,500$ spherical bubbles of radius R_{B_i} with $i \in 1, \ldots, n_{\mathrm{B}}$. The cloud is generated by randomly positioning bubbles within a sphere of radius R_{C} using a uniform distribution and subject to the constraint that the minimum distance between the surfaces of any two bubbles is greater than $d_{\mathrm{G}} = 0.4$ mm. The radius of the bubbles is chosen in the range $[R_{\mathrm{B,min}}, R_{\mathrm{B,max}}]$ using a log-normal probability distribution. The minimum and maximum bubble radii values, $R_{\mathrm{B,min}} = 0.5$ mm and $R_{\mathrm{B,max}} = 1.25$ mm, are based on the respective values suggested in Refs. [17,18]. The mean bubble radius is given by

$$\bar{R}_{\mathrm{B}} = \frac{2e^{\mu+\frac{1}{2}\sigma^2} - 1}{4}(R_{\mathrm{B,max}} - R_{\mathrm{B,min}}) + R_{\mathrm{B,min}} = 0.7 \text{ mm}, \tag{11}$$

where $\mu = 0$ and $\sigma = 0.3$ are the mean and standard deviation of the log-normal distribution, respectively. A two-dimensional sketch of the cloud setup is shown in Fig. 1. The bubble cloud is characterized by the gas volume fraction α_{C} and the cloud interaction parameter β_{C}, defined as

$$\alpha_{\mathrm{C}} = \frac{1}{R_{\mathrm{C}}^3}\sum_{i=1}^{n_{\mathrm{B}}} R_{\mathrm{B}_i}^3, \tag{12}$$

$$\beta_{\mathrm{C}} = \alpha_{\mathrm{C}}\left(\frac{R_{\mathrm{C}}}{R_{\mathrm{B,avg}}}\right)^2, \tag{13}$$

where

$$R_{\mathrm{B,avg}} = \frac{1}{n_{\mathrm{B}}}\sum_{i=1}^{n_{\mathrm{B}}} R_{\mathrm{B}_i} \tag{14}$$

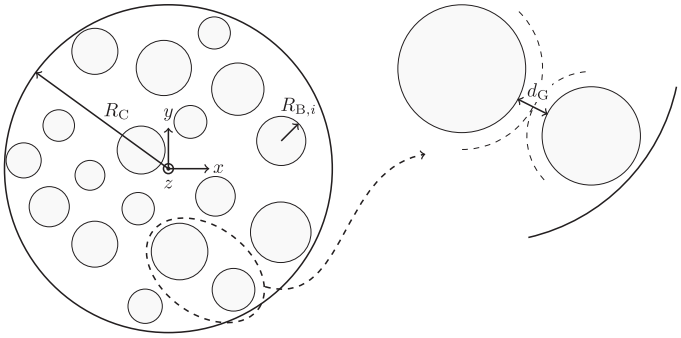

FIG. 1. Sketch of spherical cloud with radius R_C composed of bubbles with radius R_B in close-up of two bubbles separated by distance d_G.

denotes the average bubble radius. Higher β_C values indicate stronger interactions among the bubbles [13,43]. For the present cloud, $\alpha_C = 4.9\%$, $\beta_C = 208$, and $R_{B,avg} = 0.69$ mm. Figure 2 shows a histogram of the distribution of the bubble radius and a visualization of the generated cloud.

The cloud is centered in a cubic computational domain of size $6R_C \times 6R_C \times 6R_C$. The domain is uniformly discretized using $6144 \times 6144 \times 6144$ cells, leading to $R_{B,min}/h = 11.38$ for the minimum bubble resolution and $R_{B,max}/h = 28.44$ for the maximum bubble resolution, where the cell length is denoted by h. Initially, a zero velocity field is assumed. The density of water is set to $\rho_1(\mathbf{x}, t = 0) = \rho_1(0) = 1000.0\ \mathrm{kg/m^3}$ and of air to $\rho_2(0) = 1.0\ \mathrm{kg/m^3}$. Moreover, a smoothed initial pressure field [18] is used which is essential in order to attenuate the emission of spurious pressure waves caused by the initial conditions. The bubble and liquid pressure in the sphere defining the cloud is set to $p_C = 0.1$ MPa and the ambient pressure to $p_\infty = 1.0$ MPa. Following Ref. [18], the initial pressure field in the liquid outside of the cloud is then approximated via

$$p(\mathbf{x}, t = 0) = \begin{cases} p_C & \text{if } \|\mathbf{x} - \mathbf{x}_C\| \leqslant R_C, \\ p_C + \tanh\left(\frac{\|\mathbf{x}-\mathbf{x}_C\| - R_C}{\lambda}\right)(p_\infty - p_C) & \text{otherwise,} \end{cases} \tag{15}$$

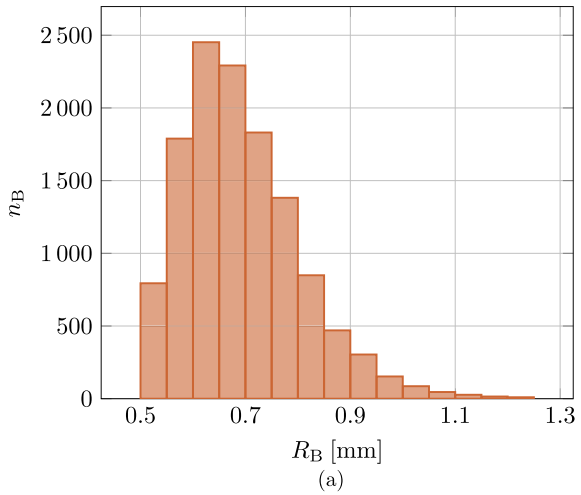

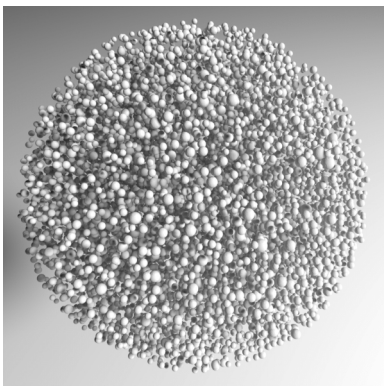
(b)

FIG. 2. (a) Distribution of bubble radius and (b) rendering of the initial cloud.

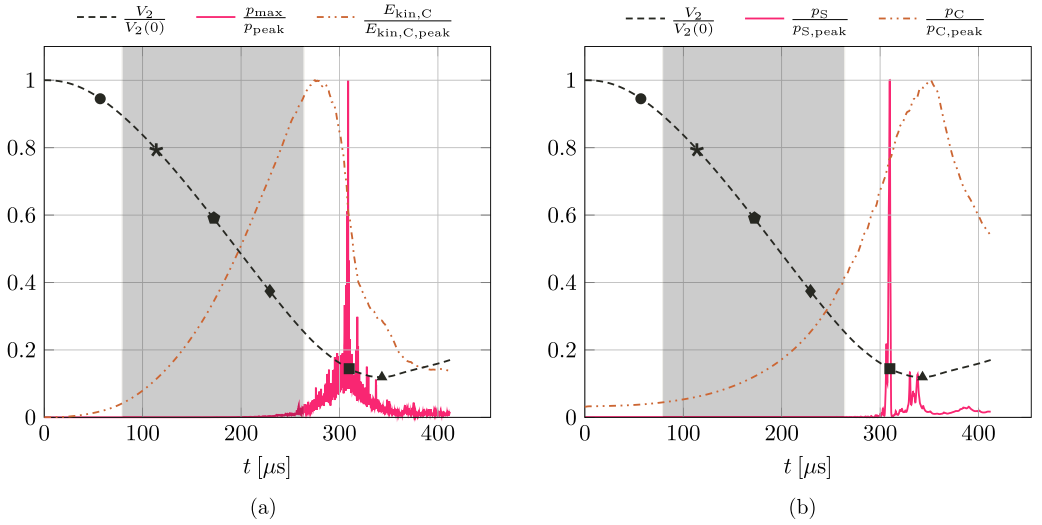

FIG. 3. Temporal evolution of (a) gas volume $V_2/V_2(0)$ together with pointwise maximum pressure $p_{\max}/p_{\text{peak}}$ within domain and average kinetic energy $E_{\text{kin,C}}/E_{\text{kin,C,peak}}$ within the cloud as well as (b) $V_2/V_2(0)$ together with average pressure $p_{\text{C}}/p_{\text{C,peak}}$ within the cloud and average pressure $p_{\text{S}}/p_{\text{S,peak}}$ within sensor at the cloud center. All quantities are normalized by their peak values. Symbols mark time instants for three-dimensional visualizations (see Fig. 4) and numerical schlieren (see Fig. 5). The gray shaded area indicates the time interval used for data extraction in the microjet analysis in Sec. IV B.

where $\mathbf{x}_{\text{C}}$ denotes the center of the cloud. Parameter λ defines how fast the pressure increases from the cloud surface to the ambient and is set to 50 mm. In Appendix B we show that the approximation described in Ref. [18] is sufficiently accurate compared to an initial condition that satisfies the Laplace equation $\nabla^2 p = 0$ for the pressure field. Nonreflecting, characteristic-based conditions [44–46] are applied at the boundaries of the computational domain. Additionally, we impose the ambient pressure p_∞ in the far field by adding the term $C_{\text{bc}}(p - p_\infty)$ to the incoming wave [47]. Coefficient $C_{\text{bc}} = \sigma(1 - \text{Ma}^2)c_1/\ell \approx \sigma c_1/\ell$ depends on a characteristic length $\ell = 3R_{\text{C}}$, the speed of sound c_1 in the liquid at the boundary, the Mach number Ma at the boundary, which is assumed negligible, and a user-defined parameter $\sigma = 0.75$s. Moreover, the CFL number is set to 0.3.

III. CLOUD COLLAPSE DYNAMICS

In this section, the cloud collapse is examined from a macroscopic point of view without considering the dynamics of the individual bubbles. The temporal evolution of characteristic quantities is provided together with visualizations of the collapsing cloud. Subsequently the propagation of the collapse wave through the cloud is analyzed and compared to predictions by Mørch's ordinary differential equation and a homogeneous mixture approach.

A. Temporal evolution and visualizations

We quantify the cloud collapse process through the temporal evolution of a number of local and global quantities. Figure 3 shows the development of the gas volume $V_2/V_2(0)$, the pointwise maximum pressure $p_{\max}/p_{\text{peak}}$ within the computational domain, the average pressure $p_{\text{C}}/p_{\text{C,peak}}$ within the cloud, the average pressure $p_{\text{S}}/p_{\text{S,peak}}$ within a sensor at the center of the cloud, further described below, and the total kinetic energy $E_{\text{kin,C}}/E_{\text{kin,C,peak}}$ within the cloud. All quantities are normalized by their peak (i.e., maximum) values. The symbols on top of the curve for the gas volume coincide with the time instants for which three-dimensional visualizations of the cloud together

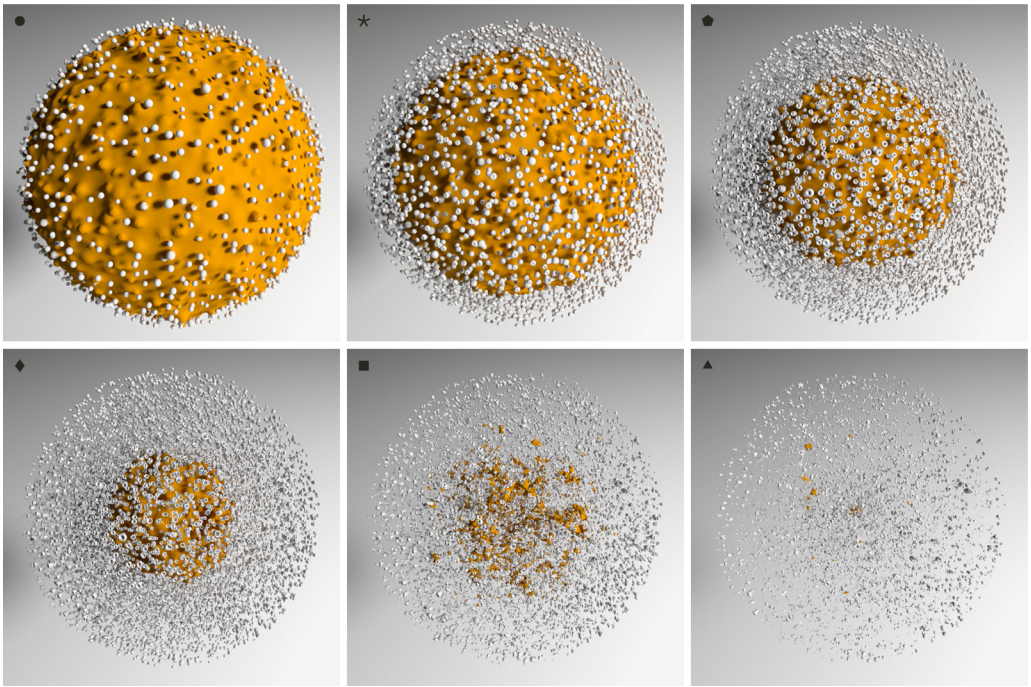

FIG. 4. Temporal evolution of collapsing cloud with pressure isosurface at $p_{\mathrm{iso}} = 0.15\,\mathrm{MPa}$. Symbols in top left corner correspond to time instants marked in Fig. 3.

with the pressure isosurface at $p_{\mathrm{iso}} = 0.15$ MPa are shown in Fig. 4 and numerical schlieren of the pressure field in the xy plane at $z = 0$ in Fig. 5. The last two symbols correspond to the time of peak pressure $p_{\mathrm{S,peak}}$ within the sensor and the time of minimum gas volume, respectively. The remaining symbols are spaced evenly between $t = 0$ and the time of occurrence of $p_{\mathrm{S,peak}}$.

The minimum gas volume is reached at time $t_{\mathrm{C}} = 343.9\ \mu$s, which is referred to as the cloud collapse time in the following. At this time, the gas volume is reduced by 88% compared to its initial value. The pointwise maximum pressure p_{max} is a highly fluctuating quantity. Its peak $p_{\mathrm{peak}} = 3.41$ GPa is detected at time $t/t_{\mathrm{C}} = 0.898$ and occurs before the minimum gas volume is encountered. A similar observation was made in Ref. [11]. To capture the behavior in the core of the cloud, we center a spherical pressure sensor of radius $R_{\mathrm{S}} = 1$ mm at the center of the cloud. The sensor measures the average pressure p_{S} over its domain. The maximum value of p_{S} amounts to $p_{\mathrm{S,peak}} = 89.5$ MPa and is observed at time $t/t_{\mathrm{C}} = 0.901$. The pressure curve of the sensor reveals the shielding effect [48,49] of the outer bubbles in the cloud. Although a broad time interval of high pressures is observed for p_{max}, merely the major peak and one smaller peak are detected by the sensor. Strong pressure waves emitted away from the immediate surrounding of the sensor are absorbed by bubbles between the source of the pressure wave and the sensor by contributing to the compression of these bubbles. The maximum value of the average pressure within the cloud is $p_{\mathrm{C,peak}} = 3.69$ MPa and significantly smaller than $p_{\mathrm{S,peak}}$. Furthermore, it is encountered at a later time $t/t_{\mathrm{C}} = 1.021$, which is almost exactly the time of minimum gas volume. The kinetic energy of the mixture in the cloud region increases until it reaches its peak value of $E_{\mathrm{kin,C,peak}} = 3.69$ J at $t/t_{\mathrm{C}} = 0.800$, which is before the occurrence of p_{peak}. At time t_{C}, the kinetic energy is already reduced by 72%.

Figure 4 illustrates the deformation of the bubbles, which is caused by the formation of microjets. As the collapse of the cloud progresses, the extracted pressure isosurface is moving inward. Accordingly, an evolving circular front is detected by the numerical schlieren of the pressure field

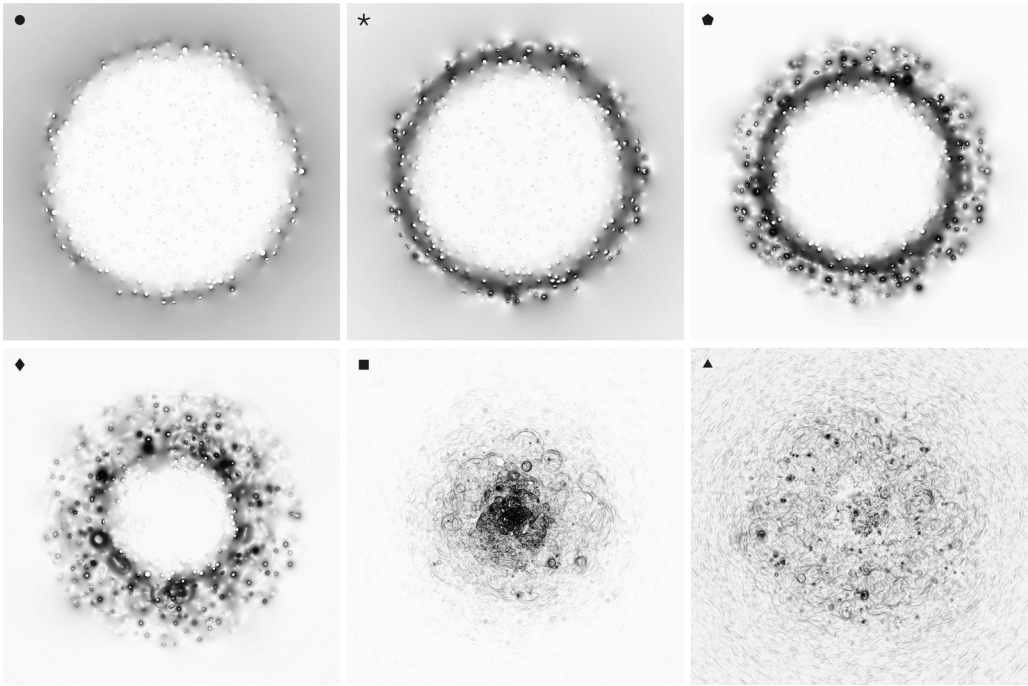

FIG. 5. Temporal evolution of collapsing cloud visualized using numerical schlieren images of the pressure field in the xy plane at $z = 0$. Symbols in top left corner correspond to time instants marked in Fig. 3.

shown in Fig. 5. Figures 4 and 5 thus reveal an inward-propagating spherical collapse wave and the aforementioned shielding effect. While the bubbles behind the front are subject to a collapse process, bubbles ahead of the front remain at their initial state. From the fourth to the fifth frame, a breakdown of the shielding effect is observed. Furthermore, strong spherical pressure waves emitted from individual bubble collapses are clearly visible in the fifth numerical schlieren frame.

B. Collapse wave propagation

The large number of bubbles in the cloud renders the macroscopic flow spherically symmetric and allows for analyzing the collapse wave observed in the previous section. Therefore, spherical averages $\bar{\alpha}_2(r,t)$, $\bar{p}(r,t)$, and $\bar{u}(r,t)$ of the gas volume fraction, the pressure and the velocity magnitude are computed over spheres with radius r centered at the cloud center. The radial position of the collapse wave front is defined by the location of the maximum average velocity magnitude as

$$R_{\mathrm{F}}(t) = \arg\max_{r} \bar{u}(r,t). \tag{16}$$

Figure 6 shows the front trajectory in the r-t space on top of a contour plot of $\bar{\alpha}_2(r,t)$ as well as the evolution of the front speed $\dot{R}_{\mathrm{F}}$, i.e., the propagation speed of the bubbly shock in the mixture [49–51]. Apart from these curves, labeled "bubbles," predictions by Mørch's ordinary differential equation and a homogeneous mixture approach which are further addressed below are also included. The propagation of the front starts immediately. The front gradually accelerates so that the front speed reaches 100 m/s at $t = 150\ \mu$s and 200 m/s at $t = 240\ \mu$s. These velocities are lower than the speed of sound in both pure fluids, which amounts to 1625 m/s for water and to 374 m/s for air under pressure $p_{\mathrm{C}} = 0.1$ MPa. Eventually, the front reaches the speed of sound of air at approximately $t = 270\ \mu$s. At about the same time, the kinetic energy of the mixture in the cloud starts to decrease and pressure disturbances penetrate the front despite the shielding effect; see Fig. 3.

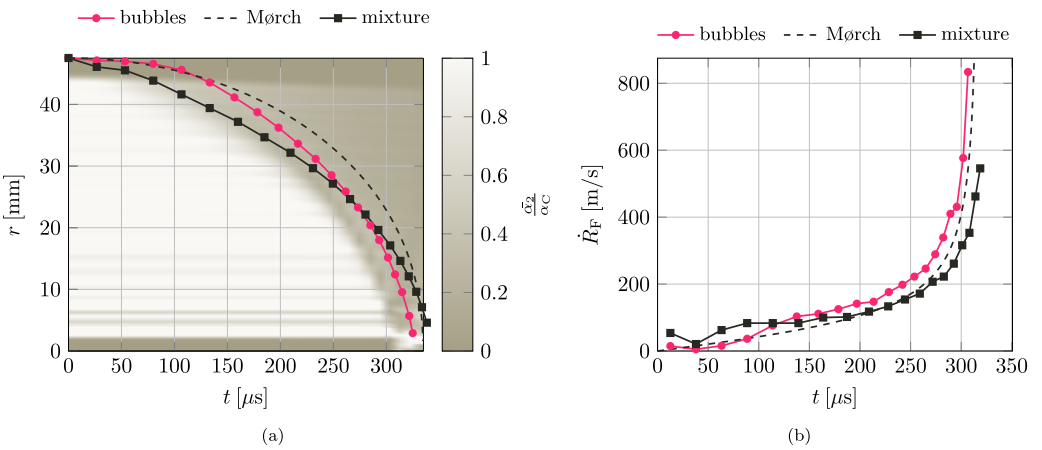

FIG. 6. (a) Front trajectory of collapse wave on $\bar{\alpha}_2$ contour plot and (b) front speed. Results obtained with the Mørch model and a homogeneous mixture approach are included for comparison.

Profiles of the spherical averages at various time instants $t = 139,\ 183,\ 218,\ 245,\ 267,\ 285,$ and 297 μs corresponding to $R_F = 40,\ 35,\ 30,\ 25,\ 20,\ 15,$ and 10 mm are shown in Fig. 7. The profiles are normalized and plotted in the frame of reference of the front, i.e., depending on the relative radial location $r - R_F(t)$. The normalized gas volume fraction, pressure, and velocity are defined as $\bar{\alpha}_2/\alpha_C$, $(\bar{p} - p_C)/(\bar{p}_F - p_C)$, and $\bar{u}/\bar{u}_F$, where $\bar{p}_F(t) = \bar{p}(R_F(t), t)$ and $\bar{u}_F(t) = \bar{u}(R_F(t), t)$ are pressure and velocity at the front. The gas volume fraction shows some oscillations which decay towards the cloud surface as more bubbles contribute to the averages with increasing r. The normalization of the radial profiles reveals their self-similarity in the vicinity of the front. The collapse wave, or bubbly shock, does not exhibit a sharp front but has a finite thickness which is related to the dynamics of the individual collapsing bubbles (see Refs. [50,52] and references therein). Consistent with the observations of the aforementioned studies, the thickness of the front is of the size of a few bubble length scales. From the velocity profiles in Fig. 7, we obtain a front thickness of approximately 10 mm, which is about seven bubble diameters. Owing to the shielding effect by the outer bubbles, all fields remain at their initial values ahead of the front, i.e., for $r - R_F < -10$ mm. Closer to the front, the gas volume fraction gradually decreases to $\alpha_2/\alpha_C \approx 0.2$ at the front, while the pressure and the velocity grow towards their peak values. Behind the front, the gas volume fraction rebounds and reaches a value of $\alpha_2/\alpha_C \approx 0.4$ at a distance of $r - R_F \approx 3$ mm. The gas volume fraction rebound behind the front [49] is accompanied by a drop in the pressure and velocity. Farther outward from the cloud center, all profiles keep declining. At the cloud surface, the gas volume fraction drops to zero in a sharp fashion, whereas pressure and velocity decrease smoothly to their prescribed far field values.

The values of the pressure and velocity at the front increase as seen from their temporal evolution shown in Fig. 8. As derived from mass and momentum balance [51,52], p_F and u_F are related to the front speed. Approximate relations for these quantities near the front are given by

$$p_F - p_C \sim \rho_1(1 - \alpha_C)\alpha_C \dot{R}_F^2, \tag{17}$$

$$u_F \sim \alpha_C \dot{R}_F \tag{18}$$

up to a scaling factor which depends on the definition of the front location. Fitting these relations to the simulation data results in

$$p_F - p_C = 6.20\,\rho_1(1 - \alpha_C)\alpha_C \dot{R}_F^2, \tag{19}$$

$$u_F = 0.75\,\alpha_C \dot{R}_F \tag{20}$$

and provides a good approximation to the present results; see Fig. 8.

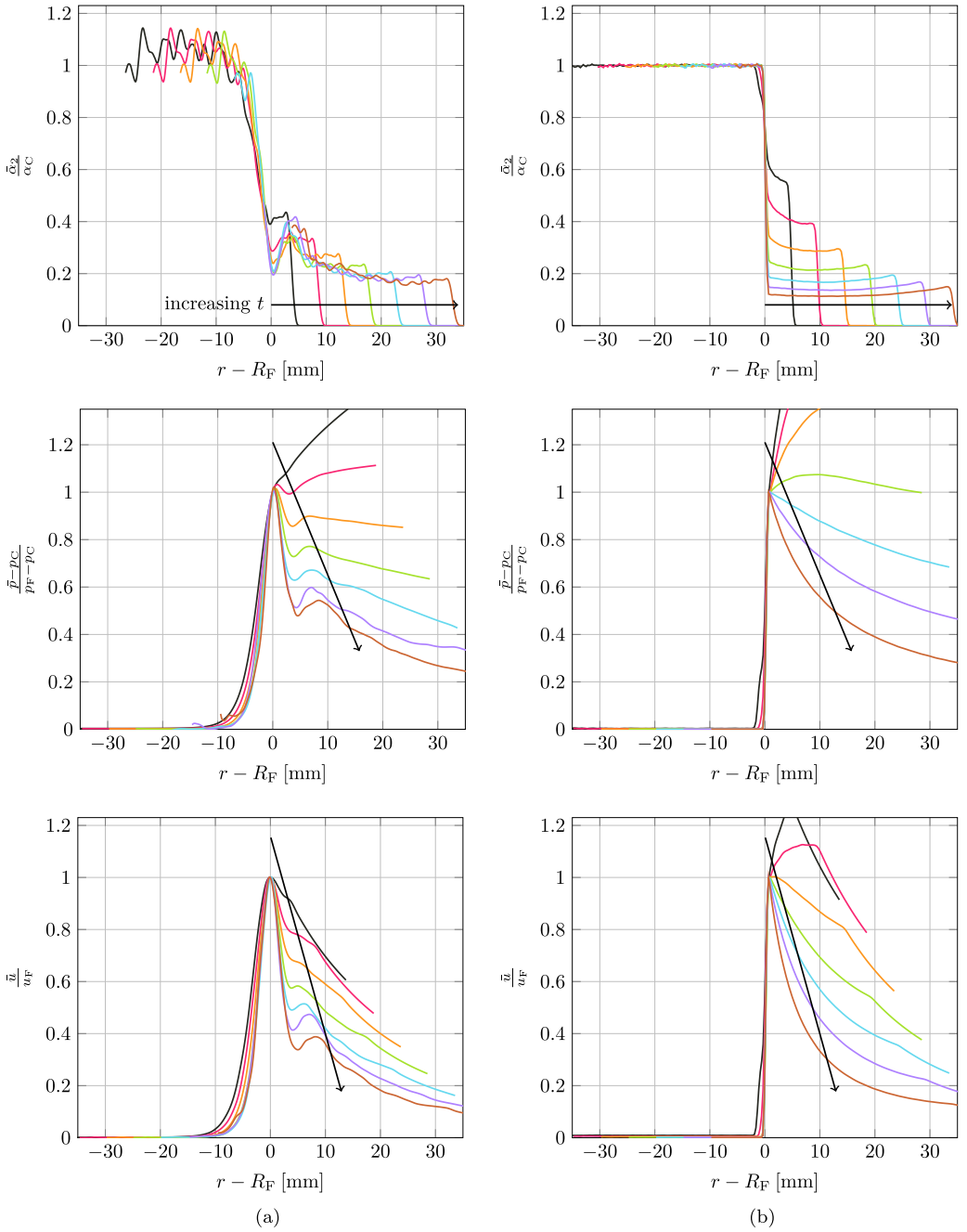

FIG. 7. Normalized profiles of spherical averages of the gas volume fraction, pressure and velocity magnitude corresponding to $R_F = 40,\ 35,\ 30,\ 25,\ 20,\ 15$, and 10 mm. Simulation with (a) resolved bubbles and (b) homogeneous mixture approach are shown. Arrows indicate increasing time.

A model proposed by Mørch in Ref. [51] describes the collapse of a spherical cloud of vapor bubbles in the form of a Rayleigh-Plesset-like equation:

$$R_F \ddot{R}_F + \left[\frac{3}{2} - \frac{1}{2}(1-\psi)(1-\alpha_C)\right]\dot{R}_F^2 = -\frac{p_\infty - p_v}{\alpha_C \rho_l}, \tag{21}$$

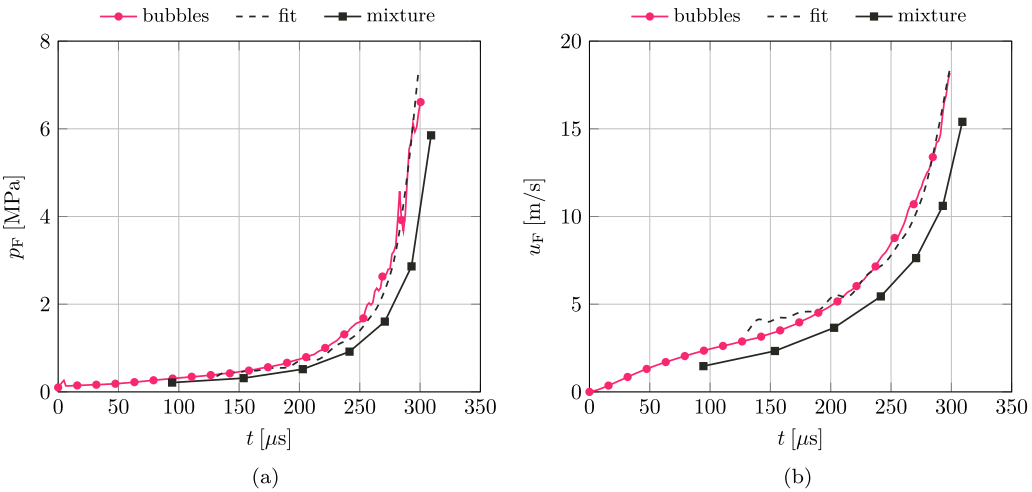

FIG. 8. (a) Temporal evolution of average pressure and (b) average velocity magnitude at the front.

where p_v denotes the vapor pressure of the liquid and ψ an energy conservation factor. The energy conservation factor accounts for energy losses due to the radiation of acoustic waves and dissipation. A larger value leads to a higher front speed. According to Ref. [51], the energy conservation factor should be in the range $0 \leqslant \psi \leqslant 0.5$. The model assumes that the bubbles are small compared to the cloud radius and that the vapor volume fraction is sufficiently high. In contrast to the present simulation of a cloud of gas bubbles, the Mørch model is derived for vapor bubbles, which means that the pressure inside the bubbles remains constant during the collapse and that the bubbles collapse completely without any rebound stage. When setting $p_v = p_C$, the Mørch model also provides a reasonable prediction for the front trajectory and speed of the present case, as can be seen from Fig. 6, where the respective curves are labeled "Mørch." For the curves shown in Fig. 6, the energy conservation factor, which is only of minor influence, is set to $\psi = 0.5$.

Furthermore, results obtained by a homogeneous mixture approach are included for comparison. Homogeneous mixture (or single-fluid) models, such as the ones proposed and/or used in Refs. [53–58], do not consider individual bubbles but treat the cloud region as a mixture of water and gas (or vapor), for instance, based on a cell-averaged void-fraction distribution. Homogeneous mixture models may be used in situations where none of the void structures are resolved on the computational grid. These situations exhibit a ratio $\bar{R}_B/h \ll 1$ of the characteristic size of the bubbles to the grid cell length. In this case, homogeneous mixture models allow the simulation of large-scale flow dynamics, i.e., dynamics that are resolvable on the chosen computational grid. By increasing the grid resolution, homogeneous mixture models are able to capture the flow dynamics of decreasingly smaller scales. The mathematical description introduced in Sec. II A may also be used to describe a homogeneous mixture of gas and liquid owing to the right-hand-side term of Eq. (5). Here we simply set a uniform gas volume fraction $\alpha_2 = \alpha_C$ for all cells within the sphere of radius R_C, instead of initially computing the cell-averaged gas-volume-fraction field from the distribution of the 12 500 bubbles in the cloud by some kind of filtering procedure. The initial conditions for the velocity and the pressure as well as the applied boundary conditions remain unchanged compared to the case with resolved bubbles. A similar approach was used in Ref. [18]. For the homogeneous mixture approach, the computational domain is discretized by 1024 cells per spatial direction. Spherically averaged profiles for $R_F = 40,\ 35,\ 30,\ 25,\ 20,\ 15$, and 10 mm corresponding to $t = 94,\ 154,\ 203,\ 242,\ 271,\ 293$, and 309 μs are shown in Fig. 7. In contrast to the case with resolved bubbles, the radial profiles are discontinuous at the front and do not demonstrate features such as the gas volume fraction rebound behind the front or the gradual

transition of the profiles ahead of the front. Therefore, the location of the collapse wave front for the homogeneous mixture case is determined from the gas volume fraction via

$$R_{\mathrm{F}}(t) = \arg\max_{r} \left| \frac{\partial \bar{\alpha}_2}{\partial t}(r,t) \right|, \tag{22}$$

which detects the discontinuity in $\bar{\alpha}_2$. The front trajectory and speed, shown in Fig. 6 by the curves labeled "mixture," are qualitatively similar to the ones of the resolved simulation. However, the front speed is underestimated starting from $t = 150$ μs, and the deviation grows in time reaching about 50 m/s at $t = 250$ μs. The temporal evolution of the pressure and the velocity at the front are included in Fig. 8. The values observed with the homogeneous mixture approach are about 30% lower compared to the resolved simulation.

In summary, our results indicate that the front trajectory and speed observed in the simulation with large numbers of bubbles are well captured by Mørch's ordinary differential equation and the present homogeneous mixture approach. The evolution of the pressure and the velocity near the front matches the theoretical relations and in turn validates the present numerical results.

IV. BUBBLE DYNAMICS

Next, the evolution of the bubbles in the cloud is examined. Their collapse behavior as well as the microjets leading to their deformation are investigated.

A. Bubble collapses

The shape of the bubbles is implicitly described by the gas-volume-fraction field α_2, which is sampled at a frequency of 0.63 MHz. The center $\mathbf{x}_{\mathrm{B}_i}(t)$ and the equivalent radius $R_{\mathrm{B}_i}(t)$ of bubble i are calculated as

$$\mathbf{x}_{\mathrm{B}_i}(t) = \frac{1}{V_{\mathrm{B}_i}(t)} \int_{\Omega_{\mathrm{B}_i}} \alpha_2 \mathbf{x} \, dV, \tag{23}$$

$$R_{\mathrm{B}_i}(t) = \left[\frac{3}{4\pi} V_{\mathrm{B}_i}(t) \right]^{1/3}, \tag{24}$$

where

$$V_{\mathrm{B}_i}(t) = \int_{\Omega_{\mathrm{B}_i}} \alpha_2 \, dV \tag{25}$$

is the bubble volume. The integration is performed over a spherical domain Ω_{B_i} concentric with the bubble center of the previous time sample and with a radius equal to the initial bubble radius $R_{\mathrm{B}_i}(0)$. In order to improve the accuracy of peak detection, the function $R_{\mathrm{B}_i}(t)$ is interpolated in time with a cubic spline.

Figure 9 shows the evolution of the equivalent bubble radius for a few bubbles selected at various radial locations. All curves are normalized by the initial bubble radius. A bubble starts to collapse once it is overtaken by the inward-propagating wave. Figure 9 illustrates that the strength of the collapses, expressed, e.g., in terms of smaller collapse times and stronger bubble compression, increases with decreasing distance to the cloud center. In the vicinity of the center of the cloud, bubbles collapse in a highly nonlinear fashion (see right column of Fig. 9), whereas they oscillate in the periphery of the cloud (see left column of Fig. 9).

B. Microjet formation

The evolving pressure gradient along the bubble surface leads to the formation of a localized liquid jet of high velocity, which notably deforms the bubble and eventually pierces though it.

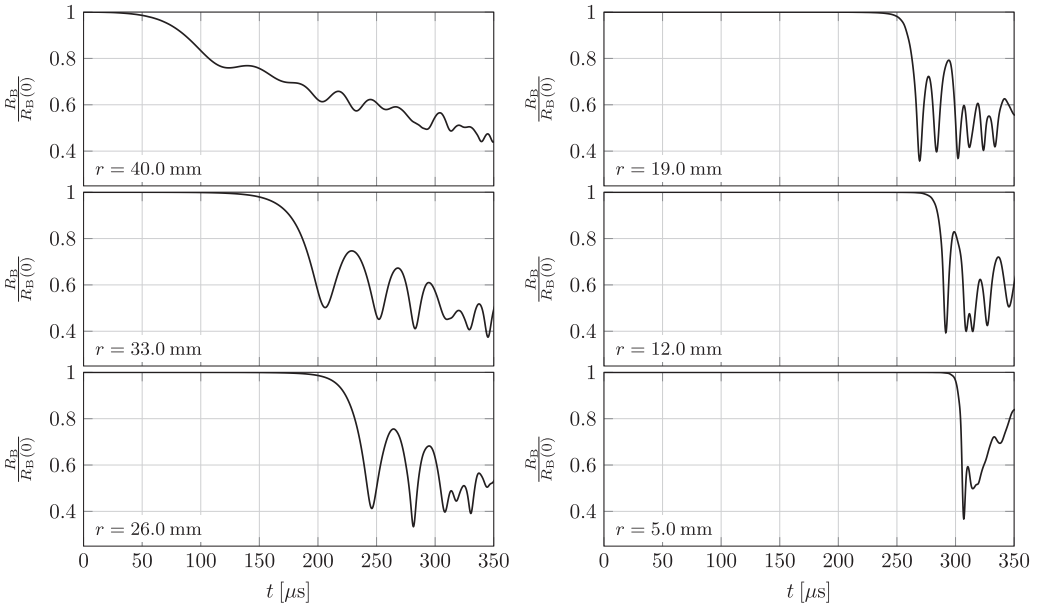

FIG. 9. Temporal evolution of equivalent radius of selected bubbles at various radial locations $r =$ 40.0, 33.0, 26.0, 19.0, 12.0, and 5.0 mm. All curves are normalized by the corresponding initial bubble radius.

Following Ref. [59], the tip $\mathbf{x}_{\mathrm{tip}_i}$ of the microjet associated with bubble i is identified as the location of minimum curvature on the bubble surface. Here the interface is represented by the isosurface $\alpha_2 = 0.5$ of the gas-volume-fraction field. The curvature of any isocontour of α_2 can be calculated from the gas-volume-fraction field via $\kappa = -\boldsymbol{\nabla} \cdot \frac{\boldsymbol{\nabla}\alpha_2}{|\boldsymbol{\nabla}\alpha_2|}$.

Figure 10 illustrates the evolution of the microjet for three bubbles. The relative location of the tip, $\mathbf{x}_{\mathrm{tip},i} - \mathbf{x}_{\mathrm{B}_i}$, as well as the bubble radius R_{B_i} are displayed as a function of time. Additionally, bubble shapes are shown for selected time instants. At the beginning of the collapse process, the bubble surface is largely spherical and possesses a positive curvature. Therefore, the distance between the location of minimum curvature and the bubble center is approximately equal to the equivalent radius, but the location itself is not well defined and thus bounces from one point to another. Once the microjet starts to form, the curvature changes its sign. The location of minimum curvature then identifies the tip of the microjet. The microjet deforms the bubble into a caplike shape until it pierces through the bubble on the opposite surface; see Fig. 10. At this time, the distance between the location of minimum curvature and the bubble center again approximately equals the equivalent radius. Hence, the characteristic quantities of the microjets are evaluated during the time interval $[t_{\mathrm{tip},i}, t_{\mathrm{imp},i}]$ for which

$$\left|\mathbf{x}_{\mathrm{B}_i} - \mathbf{x}_{\mathrm{tip},i}\right| < 0.75 R_{\mathrm{B}_i} \tag{26}$$

TABLE I. Microjet parameters of selected bubbles.

Bubble	r [mm]	θ [deg]	u_{tip} [m/s]	$R_{\mathrm{B}}(0)$ [mm]	$-\dot{R}_{\mathrm{B,min}}$ [m/s]	φ [deg]	$\lvert\hat{\mathbf{u}}^{\perp}_{\mathrm{bulk}}\rvert$
1	41.9	9.8	13.4	0.58	3.9	50.6	0.005
2	41.4	49.4	14.6	0.66	3.3	22.9	0.293
3	34.1	12.6	64.1	1.14	14.7	92.5	0.148

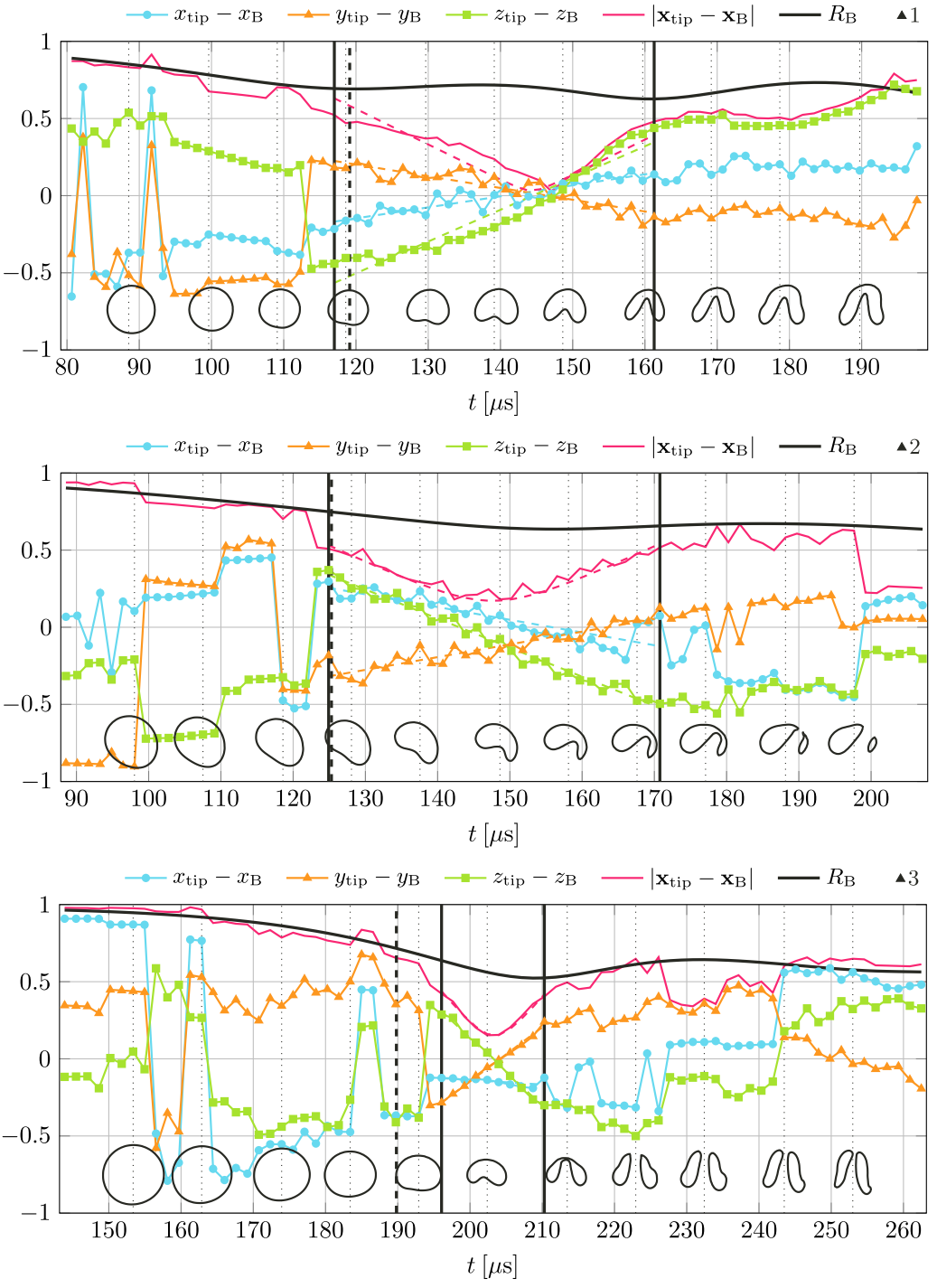

FIG. 10. Temporal evolution of microjets for three selected bubbles. Trajectory of microjet tip relative to the bubble center (solid lines), linear fit (dashed lines), and equivalent radius (black solid line). All quantities are normalized by the corresponding initial radius. Fitting range $[t_{\mathrm{tip},i}, t_{\mathrm{imp},i}]$ (vertical solid lines), collapse wave arrival t_{F} (vertical dashed line), and intervals of 10 μs with corresponding isolines of $\alpha_2 = 0.5$ at the bottom (vertical dotted lines).

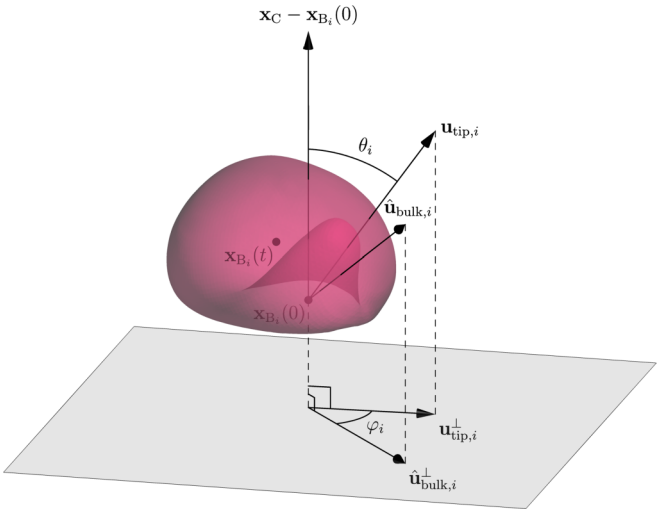

FIG. 11. Bubble surface with microjet velocity $\mathbf{u}_{\mathrm{tip},i}$ and bulk velocity indicator $\hat{\mathbf{u}}_{\mathrm{bulk},i}$ as well as their projections $\mathbf{u}^{\perp}_{\mathrm{tip},i}$ and $\hat{\mathbf{u}}^{\perp}_{\mathrm{bulk},i}$ onto a plane perpendicular to the radial direction.

holds. As observed in Fig. 10, the relative trajectory $\mathbf{x}_{\mathrm{tip},i} - \mathbf{x}_{\mathrm{B}_i}$ of the tip of the microjet travels with approximately a constant velocity within this interval. The microjet velocity $\mathbf{u}_{\mathrm{tip},i}$ is defined by the time derivative of a linear fit of $\mathbf{x}_{\mathrm{tip},i} - \mathbf{x}_{\mathrm{B}_i}$ in the time interval $[t_{\mathrm{tip},i}, t_{\mathrm{imp},i}]$. In order to obtain reliable statistics, the fitting range is required to comprise at least six samples in time (i.e., has duration of at least 10 μs) and the root-mean-square error of the fitting has to be below $0.1\,R_{\mathrm{B}_i}(0)$. Due to the limited data sampling frequency and the complexity of the microjet tip trajectories, not all bubbles satisfy these requirements. Such bubbles are excluded from the subsequent analysis of the microjets, leaving about 7500 bubbles (i.e., 60% of the bubbles) for further evaluation. The time interval that contains the microjet analyses for all bubbles is described by the interval $[t_{\mathrm{M},s}, t_{\mathrm{M},e}]$, where

$$t_{\mathrm{M},s} = \min_i(t_{\mathrm{tip},i}), \tag{27}$$

$$t_{\mathrm{M},e} = \max_i(t_{\mathrm{imp},i}) \tag{28}$$

are the start and end times, respectively. The microjet interval is highlighted in Fig. 3 with a gray shaded region. We note that the end time $t_{\mathrm{M},e}$ is before the time of minimum cloud volume t_{C}. Furthermore, Appendix A shows that the bubbles are sufficiently resolved during that time interval to guarantee at most $10.0 \pm 5.2\%$ error in the microjet velocity magnitudes relative to a grid with twice the resolution.

As reported in preceding studies on cloud collapse dynamics [9,18], the microjets point towards the core of the cloud. As shown in the present work, the axes of these microjets are not perfectly aligned with the radial direction $\mathbf{x}_{\mathrm{C}} - \mathbf{x}_{\mathrm{B}_i}(0)$ from the initial bubble center to the cloud center. The inclination angle θ_i denotes the angle between the radial direction and the direction of the microjet velocity corresponding to bubble i as illustrated in Fig. 11. A microjet with $\theta_i = 0^\circ$ is directed towards the cloud center. Values of the inclination angle for bubbles shown in Fig. 10 are given in Table I, where the microjet of bubble "2" is distinguished by stronger inclination. Figure 12 depicts a scatter plot of the inclination angle θ_i versus the radial distance r. All scatter plots shown in this subsection also contain the moving average and the standard deviation computed with a window length equal to 10% of the corresponding horizontal axis range. The bubbles selected in Fig. 10 are also marked. Furthermore, Fig. 12 depicts the probability density function (PDF) of the inclination angle. The average inclination angle for the present cloud collapse process is

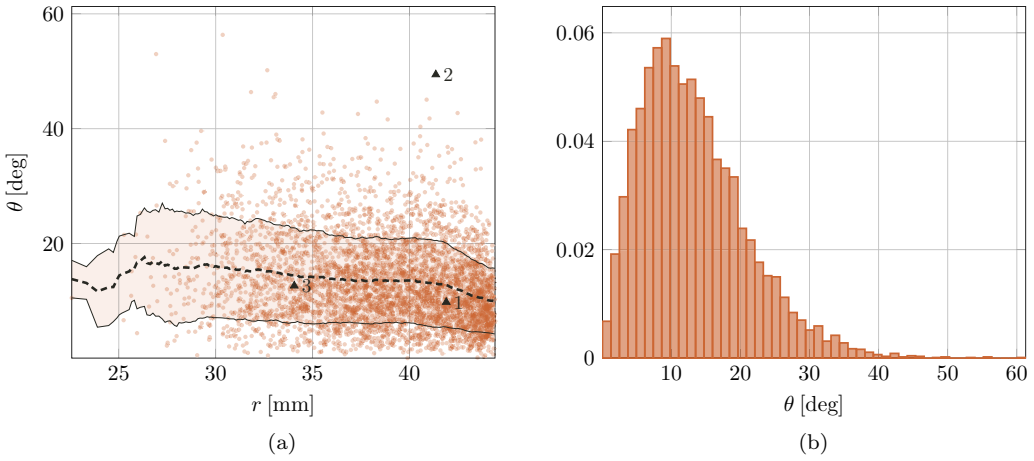

FIG. 12. (a) Microjet inclination angle θ_i depending on radial location. Moving average of the data (dashed line) is shown. Color shades indicate the standard deviation. (b) PDF of the inclination angle.

13.2°. Furthermore, 90% of the bubbles exhibit an inclination angle smaller than 24°. Local mean values of the inclination angle range from 10° at $r = 45$ mm to 18° at $r = 26$ mm. As a result, the microjet inclination angle increases slightly towards the cloud center indicating a weak dependence on the collapse wave speed, which strongly depends on r. Very large inclination angles in the range of 35° to 61° are observed for 1% of the bubbles. Closer examination of these microjets reveals that the microjet inclination is affected by the surrounding bubbles. Figure 13 shows the neighborhood of a bubble with an inclination angle of 50°. The microjet is inclined towards one specific neighboring bubble that has a significantly larger size than the considered bubble as well as all the other bubbles in its vicinity. This observation suggests that the microjet inclination mainly depends on the geometrical arrangement of the bubbles. Larger bubbles have a stronger influence on the liquid flow. Assuming potential flow away from the bubbles, the velocity in the surrounding

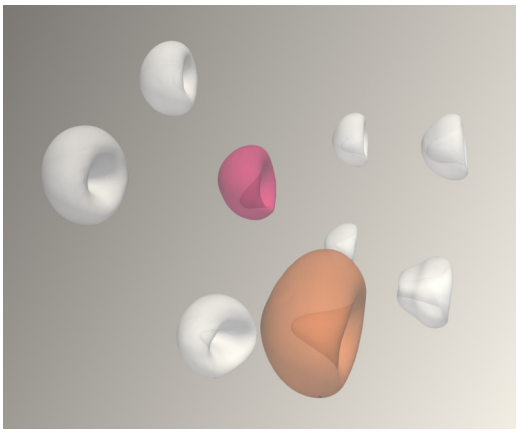

FIG. 13. Neighborhood of a small bubble (red) with a large inclination angle of 50° that is attracted towards a significantly larger bubble nearby (brown).

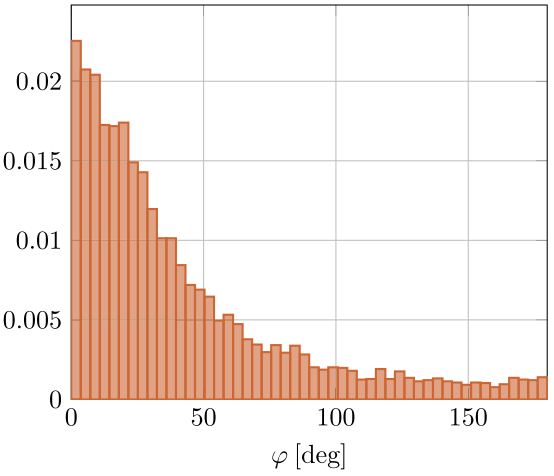

FIG. 14. PDF of angle φ_i between $\mathbf{u}^{\perp}_{\mathrm{tip},i}$ and $\hat{\mathbf{u}}^{\perp}_{\mathrm{bulk},i}$.

liquid is given by [60]

$$\mathbf{u}(\mathbf{x},t) = \sum_{j=1}^{n_B} \frac{R_{\mathrm{B}_j}^2 \dot{R}_{\mathrm{B}_j}}{\left|\mathbf{x}-\mathbf{x}_{\mathrm{B}_j}\right|^3}\left(\mathbf{x}-\mathbf{x}_{\mathrm{B}_j}\right). \tag{29}$$

Furthermore, the bubble compression rate $\dot{R}_{\mathrm{B}_j}$ in Eq. (29) is taken to be constant and negative, leading to a nondimensional bulk velocity

$$\hat{\mathbf{u}}_{\mathrm{bulk},i} = \sum_{\substack{j=1 \\ j\neq i}}^{n_B} \frac{-R_{\mathrm{B}_j}^2(0)}{\left|\mathbf{x}_{\mathrm{B}_i}(0)-\mathbf{x}_{\mathrm{B}_j}(0)\right|^3}\left[\mathbf{x}_{\mathrm{B}_i}(0)-\mathbf{x}_{\mathrm{B}_j}(0)\right] \tag{30}$$

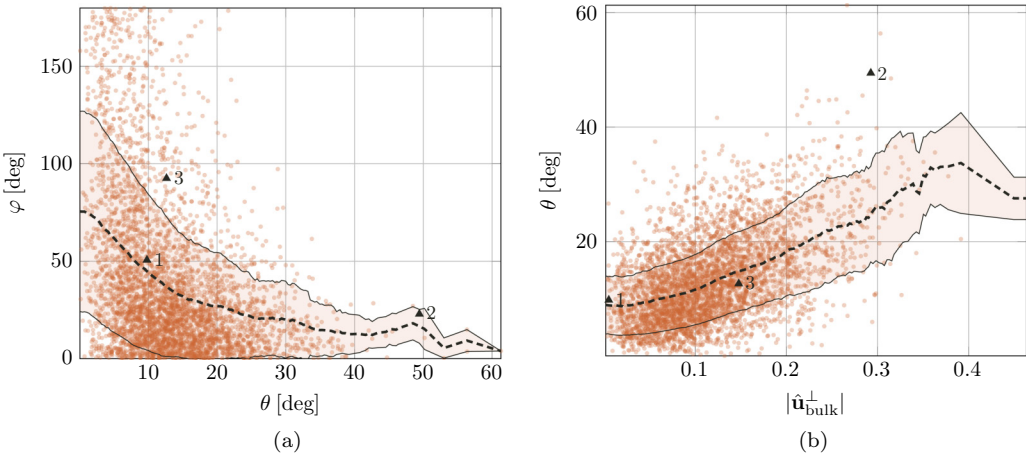

FIG. 15. (a) Angle φ_i between $\mathbf{u}^{\perp}_{\mathrm{tip},i}$ and $\hat{\mathbf{u}}^{\perp}_{\mathrm{bulk},i}$ depending on inclination angle θ_i and (b) inclination angle depending on the magnitude $|\hat{\mathbf{u}}^{\perp}_{\mathrm{bulk},i}|$. Moving average of the data (dashed line) is shown. Color shades indicate the standard deviation.

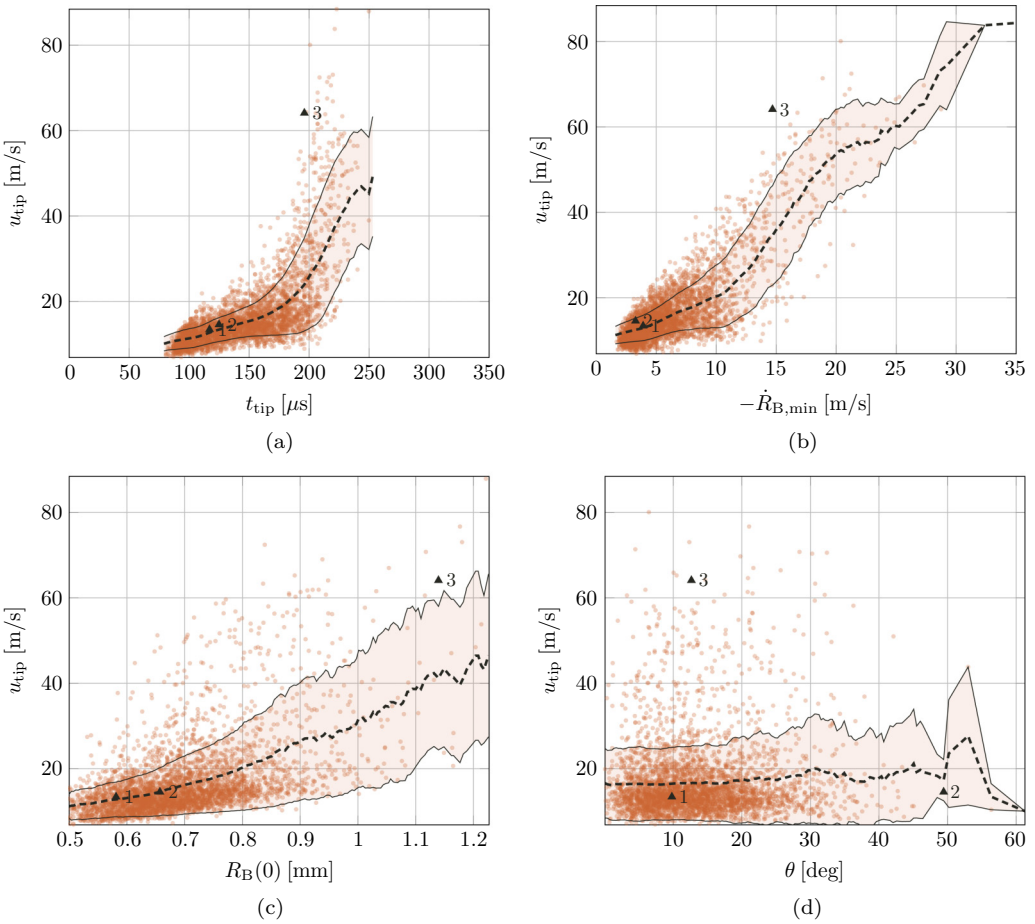

FIG. 16. Microjet tip velocity depending on (a) microjet initiation time $t_{\text{tip},i}$, (b) bubble compression rate $-\dot{R}_{\text{B}_i,\text{min}}$, (c) bubble initial radius $R_{\text{B}_i}(0)$ and (d) inclination angle θ_i. Moving average of the data (dashed line) is shown. Color shades indicate the standard deviation.

at the center $\mathbf{x}_{\text{B}_i}$ of bubble i. Equation (30) provides an estimation for the bulk flow direction and its strength which is purely based on the initial geometrical arrangement. The assumption of constant $\dot{R}_{\text{B}_j}$ does not exactly hold for cloud collapses since the bubbles behind the collapse front compress but remain at rest ahead of it. Therefore, Eq. (30) characterizes only the flow velocity perpendicular to the radial direction, which is governed by the arrangement of bubbles along the collapse front. To examine the influence of the bulk flow induced by the collapse of the surrounding bubbles on the microjet direction, $\mathbf{u}_{\text{tip},i}$ and $\hat{\mathbf{u}}_{\text{bulk},i}$ are projected onto a plane perpendicular to the radial direction. The resulting velocity components are marked by the additional superscript $(\cdot)^{\perp}$ and are also schematically represented in Fig. 11. The angle between $\mathbf{u}^{\perp}_{\text{tip},i}$ and $\hat{\mathbf{u}}^{\perp}_{\text{bulk},i}$ is denoted φ_i. The PDF of φ_i as well as scatter plots of φ_i versus θ_i and θ_i versus the magnitude $|\hat{\mathbf{u}}^{\perp}_{\text{bulk},i}|$ of the projected bulk velocity are shown in Figs. 14 and 15, respectively. For 68% of the bubbles, φ_i is smaller than 45°, which demonstrates that the microjets are inclined towards the direction of the bulk liquid flow around the bubble. This angle reduces with increasing inclination. The mean value of φ_i is 45° for $\theta_i = 10°$ and 25° for $\theta_i = 40°$. Moreover, a positive correlation between the inclination angle θ_i and the magnitude of the projected component of the bulk flow indicator $|\hat{\mathbf{u}}^{\perp}_{\text{bulk},i}|$ is observed.

Figure 16 displays scatter plots of the microjet velocity magnitude depending on various quantities. The velocity magnitude of the microjets increases with their time of initiation. For instance, the mean value amounts to 10 m/s for $t_{\mathrm{tip}} = 80\ \mu$s and to 50 m/s for $t_{\mathrm{tip}} = 250\ \mu$s. This behavior is consistent with the acceleration of the collapse wave and the growth of the pressure at the front. One of the fastest microjets is observed for bubble "3" included in Fig. 10 and Table I. The scatter plot of the microjet velocity magnitude versus the initial bubble radius $R_B(0)$ shows that larger bubbles exhibit faster microjets. The mean value rises from 20 to 40 m/s for bubbles with an initial radius between 0.5 and 1.2 mm. Another quantity relevant to the collapse strength of a bubble is the peak compression rate $-\dot{R}_{\mathrm{B}_i,\mathrm{min}}$ which is evaluated within the time interval $[t_{\mathrm{tip},i}, t_{\mathrm{imp},i}]$. A positive correlation of the compression rate with the magnitude of the microjet velocity is observed in Fig. 16. In contrast, the inclination angle θ_i does not affect the magnitude of the microjet velocity. The analyzed relations reveal that the microjet velocity is influenced by both parameters of individual bubbles (e.g., the initial bubble radius) and macroscopic parameters of the cloud collapse (e.g., the collapse front speed). However, the overall large dispersion of these relations indicates the influence of further factors such as the spatial configuration of the surrounding bubbles.

V. CONCLUSIONS

We have presented the results from state-of-the-art simulations of the collapse of a spherical cloud of 12 500 gas-filled bubbles, corresponding to a gas volume fraction of 4.9%. This cloud composed by many small bubbles allows for proper averaging over the global system and enables a large sample count for reliable statistics on the scale of the bubbles. To capture the dynamics of the bubbles, i.e., their interactions and deformations, a diffuse interface finite volume method that represents the bubbles on the computational grid has been applied.

Starting from a macroscopic point of view, we have examined the collapse process, which starts at the surface of the cloud and then propagates inward focusing in the core of the cloud. We have calculated spherical averages of the gas-volume fraction, pressure, and velocity-magnitude fields and have identified the collapse wave front. The collapse wave front advances in accordance with Mørch's ordinary differential equation and a homogeneous mixture approach. In contrast to these models, the detailed simulation discloses the thickness of the collapse wave front, which is of the order of a few bubble diameters. Furthermore, we have examined the bubbles individually. We have analyzed their collapse behavior and have used their deformation to recover the microjets. Our investigations have revealed that the microjets do in general not exactly point towards the cloud center. For the present cloud configuration, they are inclined to an angle up to 50° with respect to the radial direction. Closer examinations have demonstrated the correlation between this inclination and the bubble distribution in the vicinity of the microjets. For the velocity at the tip of the microjet, we have observed correlations with the radial location and the size of the bubble from which the microjet has been extracted.

ACKNOWLEDGMENTS

We gratefully acknowledge a number of awards for computer time that made these large-scale simulations possible. Computer time was provided by the Innovative and Novel Computational Impact on Theory and Experiment (INCITE) program under the project CloudPredict. This research used resources of the Argonne Leadership Computing Facility, which is a DOE Office of Science User Facility supported under Contract DE-AC02-06CH11357. We acknowledge PRACE for awarding us access to Fermi (CINECA, Italy) with project Pra09_2376 and Juqueen (Jülich Supercomputing Centre, Germany) with project PRA091. This work was also supported by a grant from the Swiss National Supercomputing Centre (CSCS) under Project ID s500 and s754. All provided computational resources are gratefully acknowledged.

APPENDIX A: GRID RESOLUTION ASSESSMENT

In this Appendix, we show convergence results for the macroscopic and microscopic scales that are involved in the collapse process of a cloud of gas bubbles. We start with a scaling argument for the variables that determine the dynamics of the problem in order to arrive at expressions which allow us to select a proper cloud configuration to perform the study with a reduced computational budget. The following variables are included in the scaling argument:

(1) Liquid and gas densities ρ_k with $k \in \{1, 2\}$
(2) Liquid and gas sound speeds c_k with $k \in \{1, 2\}$
(3) Initial bubble and liquid pressure p_C in the sphere defining the cloud (refer to Sec. II C)
(4) Initial gas volume fraction of the cloud α_C
(5) Initial cloud and mean bubble radii R_C and $\bar{R}_B$, respectively

The mean bubble radius $\bar{R}_B$ is defined in Eq. (11).

We nondimensionalize the variables following the approach presented in Ref. [61], where a physically significant quantity q is written as $q = q^* \tilde{q}$ with q^* its characteristic dimensional value and $\tilde{q}$ its nondimensional value. The problem is further simplified by the following two assumptions:

(1) The inertia of the gas is neglected ($\rho_2 \ll \rho_1$),
(2) The liquid is treated as incompressible ($c_1 \to \infty$).

We set $\tilde{\rho}_1 = 1.0$, $\tilde{c}_2 = 1.0$, $\tilde{R}_B = 1.0$ and obtain the following characteristic values:

$$\rho^* = \frac{\rho_1}{\tilde{\rho}_1} = 1000.0\ \mathrm{kg/m^3}, \quad c^* = \frac{c_2}{\tilde{c}_2} = \sqrt{\frac{\gamma_2 p_C}{\rho_2}} = 374.2\ \mathrm{m/s}, \quad R^* = \frac{\bar{R}_B}{\tilde{R}_B} = 0.7 \times 10^{-3}\ \mathrm{m}. \tag{A1}$$

The remaining nondimensional numbers for the cloud radius, pressure and gas volume fraction are then obtained by

$$\tilde{R}_C = \frac{R_C}{R^*}, \quad \tilde{p} = \frac{p}{p^*}, \quad \alpha_C, \tag{A2}$$

respectively, where the characteristic pressure $p^* = p_C$ is obtained from $c^* = \sqrt{\gamma_2 p^*/\rho_2}$ and p is a reference pressure. We estimate the characteristic timescale of the bubble dynamics with $t_B^* \sim 1/f_B$, where the bubble oscillation frequency f_B is given by

$$f_B = \frac{1}{2\pi \bar{R}_B} \sqrt{\frac{3\gamma_2 p}{\rho_1}}; \tag{A3}$$

see Ref. [62]. By substituting scaled variables we obtain

$$t_B^* \sim \frac{1}{f_B} \sim \bar{R}_B \sqrt{\frac{\rho_1}{\rho_2}\frac{\rho_2}{p}} \sim \frac{R^*}{c^*} \tilde{R}_B \sqrt{\frac{1}{\tilde{p}}}\ \ [\mathrm{s}]. \tag{A4}$$

For the macroscopic timescale of the cloud collapse, t_C^*, we estimate the front speed $\dot{R}_F \sim \sqrt{p/[\rho_1(1-\alpha_C)\alpha_C]}$ based on Eq. (17) and proceed similarly as above:

$$t_C^* \sim \frac{R_C}{\dot{R}_F} \sim R_C \sqrt{\frac{\rho_1}{\rho_2}\frac{\rho_2}{p}(1-\alpha_C)\alpha_C} \sim \frac{R^*}{c^*} \tilde{R}_C \sqrt{\frac{(1-\alpha_C)\alpha_C}{\tilde{p}}}\ \ [\mathrm{s}]. \tag{A5}$$

The ratio of the two timescales yields

$$\frac{t_C^*}{t_B^*} \sim \frac{\tilde{R}_C}{\tilde{R}_B} \sqrt{(1-\alpha_C)\alpha_C} \sim \sqrt{\beta_C}, \tag{A6}$$

TABLE II. Overview of altered simulation parameter for the resolution assessment study.

Case	n_B	R_C [mm]	$R_{B,avg}$ [mm]	α_C [%]	t_C^*/t_B^*
Production run	12 500	45	0.69	4.9	13.9
Grid refinement	400	9	0.64	15.2	4.6

which is identical to the result shown in Ref. [13]. Estimates for the characteristic microjet tip velocity and front speed are obtained from Eqs. (A4) and (A5), respectively:

$$u_{tip}^* \sim \frac{R^*}{t_B^*} \sim c^* \frac{1}{\tilde{R}_B}\sqrt{\tilde{p}} \text{ [m/s]}, \tag{A7}$$

$$\dot{R}_F^* \sim \frac{R^*}{t_C^*} \sim c^* \frac{1}{\tilde{R}_C}\sqrt{\frac{\tilde{p}}{(1-\alpha_C)\alpha_C}} \text{ [m/s]}. \tag{A8}$$

We choose a simulation setup for the resolution assessment based on Eqs. (A7) and (A8). Velocity microscales are retained by configuring a bubble cloud with an identical log-normal distribution for the bubble radii as well as preserving the pressure ratio $\tilde{p}$ based on a reference pressure $p = p_\infty$; refer to Sec. II C. Taking into account a reduced computational budget, the cloud radius R_C and gas volume fraction α_C cannot be preserved. Changing these parameters will affect only the macroscopic scales for which convergence is achieved faster, even on coarse grids. For these reasons, we use a bubble cloud with radius $R_C = 9$ mm and $n_B = 400$ bubbles, which yields a gas volume fraction of $\alpha_C = 15.2\%$. All other parameters remain unchanged and correspond to their definitions in Secs. II A and II C. Table II shows the simulation parameters that are changed for the resolution assessment. The computational cost is further reduced by a symmetry approximation such that only one octant of the full computational domain is simulated. Symmetry boundary conditions are used for boundaries that intersect the cloud, where the remaining boundary conditions are identical to Sec. II C. The center of bubbles that initially intersect one of the symmetry planes has been shifted onto the intersecting plane such that the bubble is initially symmetric with respect to that plane. The cloud in the octant is then extracted from the full cloud. Figure 17 shows the temporal evolution of the gas volume $V_2/V_2(0)$ and the average kinetic energy $E_{kin,C}/E_{kin,C,peak}$ within the cloud corresponding to the grid refinement parameter shown in Table II. The cloud collapse time for this configuration is $t_C = 115.9$ μs; a 2.97 times faster collapse compared to the time reported in Sec. III A. In contrast, Eq. (A5) estimates a 3.01 times faster cloud collapse time. Furthermore, Fig. 17 shows the result for the simulation using the aforementioned symmetry approximation, which results in a slightly faster cloud collapse time. The difference stems from the mirroring of the random cloud in the octant on the symmetry planes, which does not exactly match the full random cloud in the remaining octants. The resulting relative error in the cloud collapse time is 3.8% and does not affect the order of magnitude of the macroscopic timescale. The reduction in computational cost clearly outweighs the small error incurred by this approximation. Microscopic scales, described by Eq. (A4), remain in the same order of magnitude for all clouds presented in the paper.

Three grid resolutions G_-, G_0, and G_+ are used, where G_0 corresponds to the initial bubble resolution described in Sec. II C. The resolution on the coarse grid G_- is half of G_0 and the resolution on the fine grid G_+ is twice the resolution of G_0. Table III shows the three grids used for the resolution assessment including the number of cells N along each edge of the octant and the initial number of cells per radius for the smallest and largest bubbles in the cloud. Due to the symmetry assumption, the cloud is centered at the domain origin with domain extents $3R_C \times 3R_C \times 3R_C$ for the x, y, and z coordinates, respectively. Figure 18 compares the temporal evolution of the gas volume $V_2/V_2(0)$ and the average kinetic energy $E_{kin,C}/E_{kin,C,peak}$ within the cloud for the three different resolutions. Geometric quantities such as the gas volume already converge on the coarse grid G_-. Only a weak grid dependence is identified during the postcollapse of the cloud where small

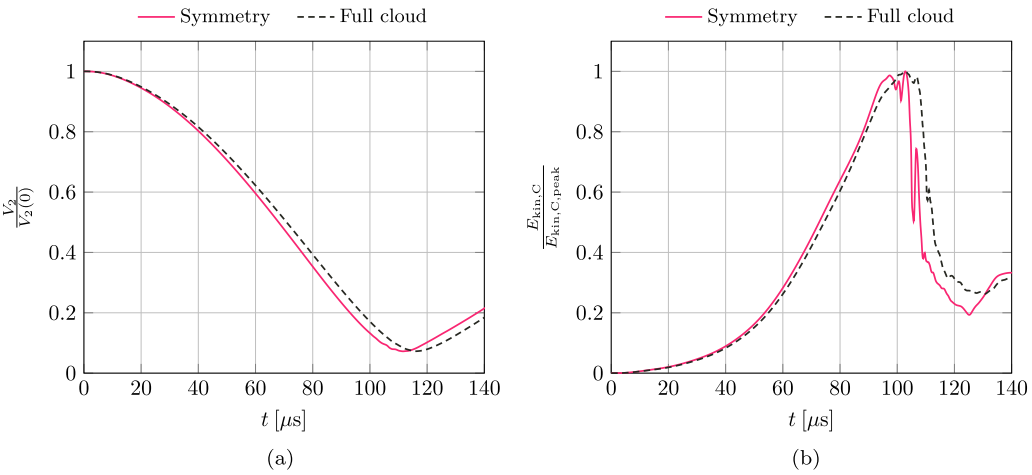

FIG. 17. Temporal evolution of (a) gas volume $V_2/V_2(0)$ and (b) average kinetic energy $E_{\mathrm{kin,C}}/E_{\mathrm{kin,C,peak}}$ within the cloud. Full cloud simulation (black dashed lines) and reduced domain approximation with symmetry boundaries (red solid lines).

length scales are dominant. Stronger grid dependence is observed for velocity and quantities that depend on it. This dependence is mainly restricted to the region after the minimum cloud volume has been reached due to its sensitivity on numerical diffusion at smaller scales. The analyses presented in this paper do not depend on data after t_{C} and, therefore, are not critical. During the cloud collapse we observe convergence for the integral of kinetic energy on grid G_0. The reduced cloud used for this grid refinement study consists of 62 bubbles where 49 bubbles (79%) satisfy the quality criteria for the microjet evaluation on all three grids; see Sec. IV B. The characteristic quantities are evaluated within the time interval $[t_{\mathrm{tip},i}, t_{\mathrm{imp},i}]$ for bubble i. The start and end time that covers the microjet analyses for all bubbles, $t_{\mathrm{M},s}$ and $t_{\mathrm{M},e}$, respectively, are furthermore shown in Table III for each grid; refer to Eqs. (27) and (28).

1. Characteristic microjet quantities

Figure 19 shows the microjet velocity magnitudes and the inclination angles computed on the three different resolutions. The data for G_+ are sorted in increasing order, while the data for G_0 and G_- are shown relative to that sort order. The gray shaded region in Fig. 18 highlights the interval $[t_{\mathrm{M},s}, t_{\mathrm{M},e}]$, which corresponds to the time range of the displayed data in Fig. 19. Table IV shows absolute errors relative to the fine grid G_+ for the microjet velocity magnitude $u_{\mathrm{tip},i}$, inclination angle θ_i and the fit range $[t_{\mathrm{tip},i}, t_{\mathrm{imp},i}]$ averaged over all bubbles. The microjet velocity magnitudes on the production grid G_0 are within a $10.0 \pm 5.2\%$ error margin relative to the fine grid G_+. The errors reported in Table IV suggest that only a marginal accuracy improvement can be achieved when doubling the resolution of the production run and does not justify the 16-fold increase in computational cost that is associated with it in regard to the scope of our analyses.

TABLE III. Grid resolutions used for the refinement study.

Grid		N	$R_{\mathrm{B,min}}/h$	$R_{\mathrm{B,max}}/h$	$t_{\mathrm{M},s}$ [μs]	$t_{\mathrm{M},e}$ [μs]
G_-	(coarse)	448	8	14	42.3	103.6
G_0	(production)	896	16	28	40.3	98.4
G_+	(fine)	1792	33	57	39.9	98.8

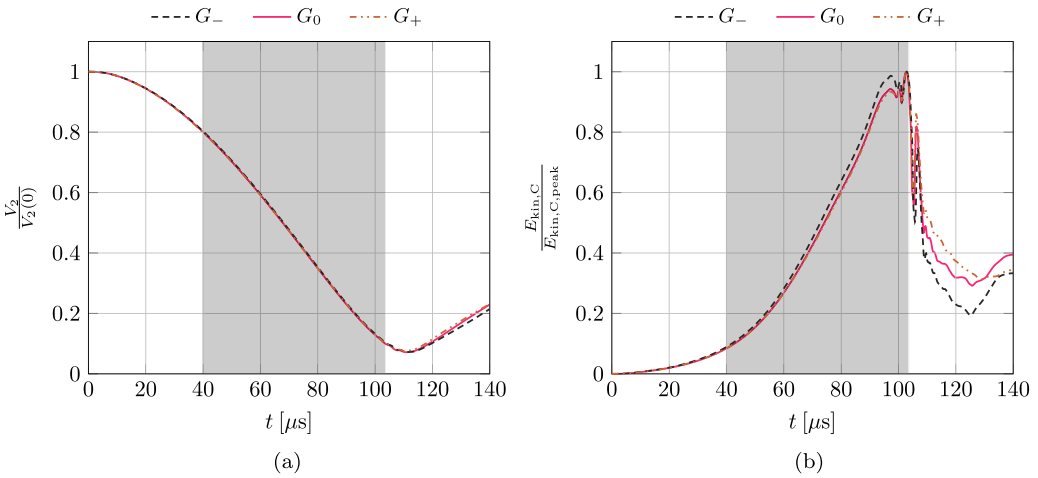

FIG. 18. Temporal evolution of (a) gas volume $V_2/V_2(0)$ and (b) average kinetic energy $E_{\mathrm{kin,C}}/E_{\mathrm{kin,C,peak}}$ within the cloud for the three resolutions shown in Table III. The gray shaded area corresponds to the time interval of the data displayed in Fig. 19.

Moreover, microjet velocity magnitudes are between 10 m/s and 60 m/s; see Figs. 16 and 19. These characteristic velocities relate to the length scale imposed by the mean bubble radius $\bar{R}_\mathrm{B}$ defined in Eq. (11). Based on these quantities, as well as the kinematic viscosity $\nu = 1.0 \times 10^{-6}$ m^2/s for water, we expect Reynolds numbers in the range 7000–42 000. Similarly, the Weber number is in the range of 972–35 000 based on a surface tension coefficient of 0.072 N/m for air-water systems. Both of these ranges justify the neglect of viscous and surface tension forces, respectively.

Figure 20 shows the temporal evolution of the normalized bubble radius $R_\mathrm{B}/R_\mathrm{B}(0)$ as well as the normalized interface thickness $[d_\mathrm{I} - d_\mathrm{I}(0)]/d_\mathrm{I}(0)$ for the collapse of a single air bubble in water

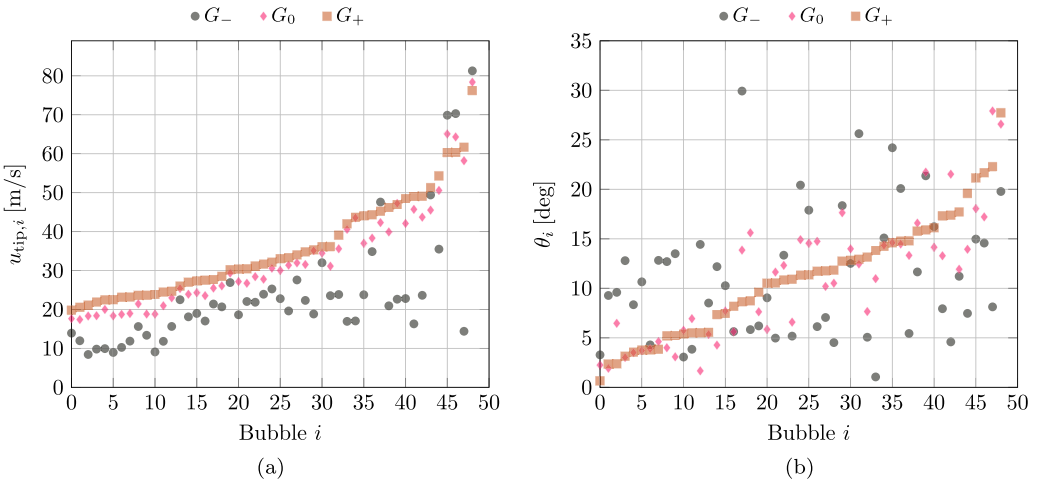

FIG. 19. (a) Microjet velocity magnitude $u_{\mathrm{tip},i}$ and (b) microjet inclination angle θ_i of individual bubbles i for the three resolutions shown in Table III. Both quantities clearly indicate convergence towards the finest grid G_+.

TABLE IV. Absolute errors averaged over all bubbles relative to the fine grid G_+.

Grid		$u_{\mathrm{tip},i}$ [m/s]	θ_i [deg]	$t_{\mathrm{tip},i}$ [μs]	$t_{\mathrm{imp},i}$ [μs]	$T_{\mathrm{B},i}$ [μs]
G_-	(coarse)	13.0 ± 8.6	6.4 ± 4.1	1.7 ± 0.9	11.1 ± 6.4	0.41 ± 0.46
G_0	(production)	3.2 ± 1.6	2.4 ± 2.0	1.0 ± 1.1	2.7 ± 1.8	0.24 ± 0.21

[31]. The interface thickness is defined by

$$d_{\mathrm{I}} = R_{\theta=0.1} - R_{\theta=0.9} \tag{A9}$$

based on two equivalent bubble radii. These radii are associated with the 0.1- and 0.9-isocontours of the gas-volume-fraction field α_2. The equivalent bubble radius is defined by $R_\theta = h\sqrt[3]{3/(4\pi)\sum_{l=1}^{n_c}\chi_\theta}$ and uses a shifted phase indicator function χ_θ with threshold value θ, which is given by $\chi_\theta = 1$ if $\alpha_2 > \theta$ and $\chi_\theta = 0$ otherwise. In the definition of R_θ, h denotes the cell size and n_c the number of grid cells. We use the Keller-Miksis [63] solution as a reference for the validation of our numerical results in Fig. 20(a). Numerical solutions based on Eqs (1)–(5) are obtained on two grid resolutions that correspond to the resolution of the smallest and largest bubbles in our present 12 500 bubble cloud. We further emphasize the influence of the "K-div," term which corresponds to the source term $K\nabla \cdot \mathbf{u}$ in Eq. (5). Including the K-div term in the model improves the accuracy of the numerical result considerably, even at rather low resolutions. A similar trend is observed in the evolution of the interface thickness in Fig. 20(b). The thickness of the interface increases strongly when the bubble reaches its minimum radius for simulations that do not include the K-div term in the model, while an approximate linear increase of the interface thickness is observed for the case including the K-div term. This linear increase can be attributed almost exclusively to numerical diffusion. A recent study [64] further extends this analysis by including a pressure-disequilibrium model applied to spherical single-bubble collapse.

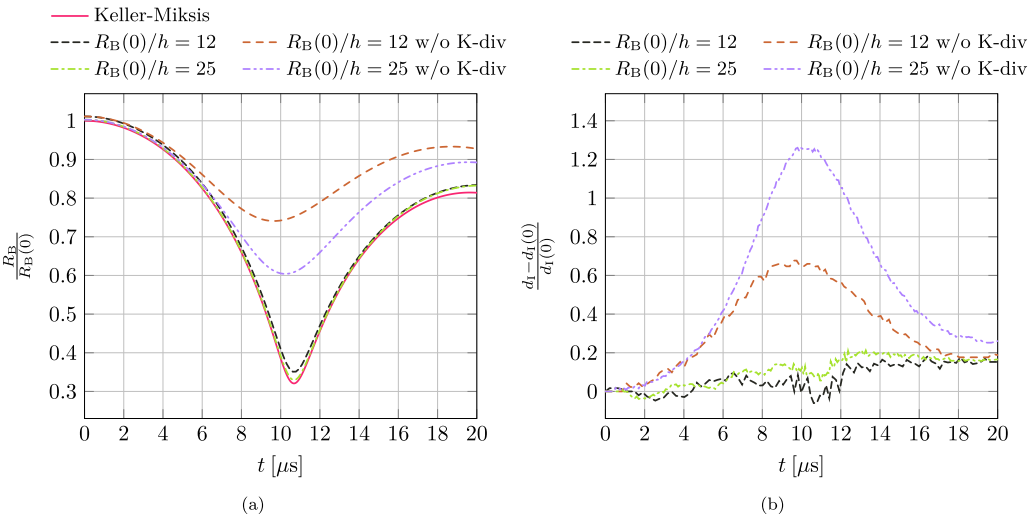

FIG. 20. Collapse of a single air bubble in water at different resolution. (a) Evolution of bubble radius R_{B} and (b) evolution of interface thickness d_{I}. Extracted from Ref. [31].

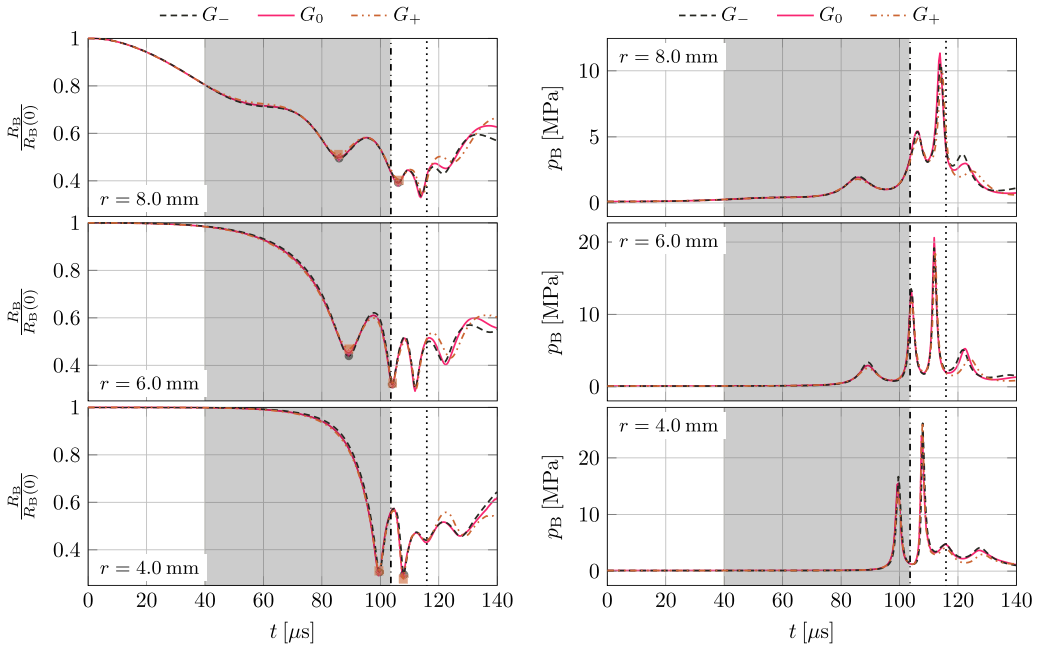

FIG. 21. Temporal evolution of (a) equivalent radius $R_B/R_B(0)$ and (b) average bubble pressure p_{B_i} of selected bubbles at radial locations $r = 8.0$, 6.0, and 4.0 mm for the three resolutions shown in Table III. The vertical lines indicate the end of the microjet evaluation interval $t_{M,e}$ (vertical dash-dotted line) and the time of minimum cloud volume t_C (vertical dotted line), respectively. First and second minimum locations of the equivalent radius are indicated for G_- (circles), G_0 (diamonds), and G_+ (squares).

2. Collapse period and bubble pressure

Figure 21 shows the temporal evolution the equivalent bubble radius, Eq. (24), and average bubble pressure for three selected bubbles. The computation of the average bubble pressure follows the same approach used for the bubble center $\mathbf{x}_{B_i}$ in Eq. (23). It is defined by

$$p_{B_i}(t) = \frac{1}{V_{B_i}(t)} \int_{\Omega_{B_i}} \alpha_2 p \, dV, \tag{A10}$$

where the bubble volume $V_{B_i}(t)$ is defined in Eq. (25). Data for the three resolutions described in Table III are included in each plot. The location of the first and second minima of the equivalent bubble radius is not sensitive to the grid resolution. This observation is in correspondence with the previous statement regarding geometric quantities. The bubble collapse period T_B is derived from the equivalent bubble radius and is associated with a $1.8 \pm 1.7\%$ error margin on grid G_0 relative to the fine grid G_+. Absolute error values averaged over all bubbles are shown in Table IV. The

TABLE V. L_2 error measures for R_{B_i} and p_{B_i} averaged over all bubbles. The values correspond to the time intervals $[0, t_{M,e}]$ and $[t_{M,e}, t_C]$, respectively, expressed as percentage error relative to the fine grid G_+.

Grid		$L_2(R_{B_i}; 0, t_{M,e})$	$L_2(R_{B_i}; t_{M,e}, t_C)$	$L_2(p_{B_i}; 0, t_{M,e})$	$L_2(p_{B_i}; t_{M,e}, t_C)$
G_-	(coarse)	1.1 ± 0.4	3.3 ± 1.6	4.9 ± 1.6	15.7 ± 10.0
G_0	(production)	0.6 ± 0.09	2.8 ± 0.9	2.4 ± 0.5	13.2 ± 5.8

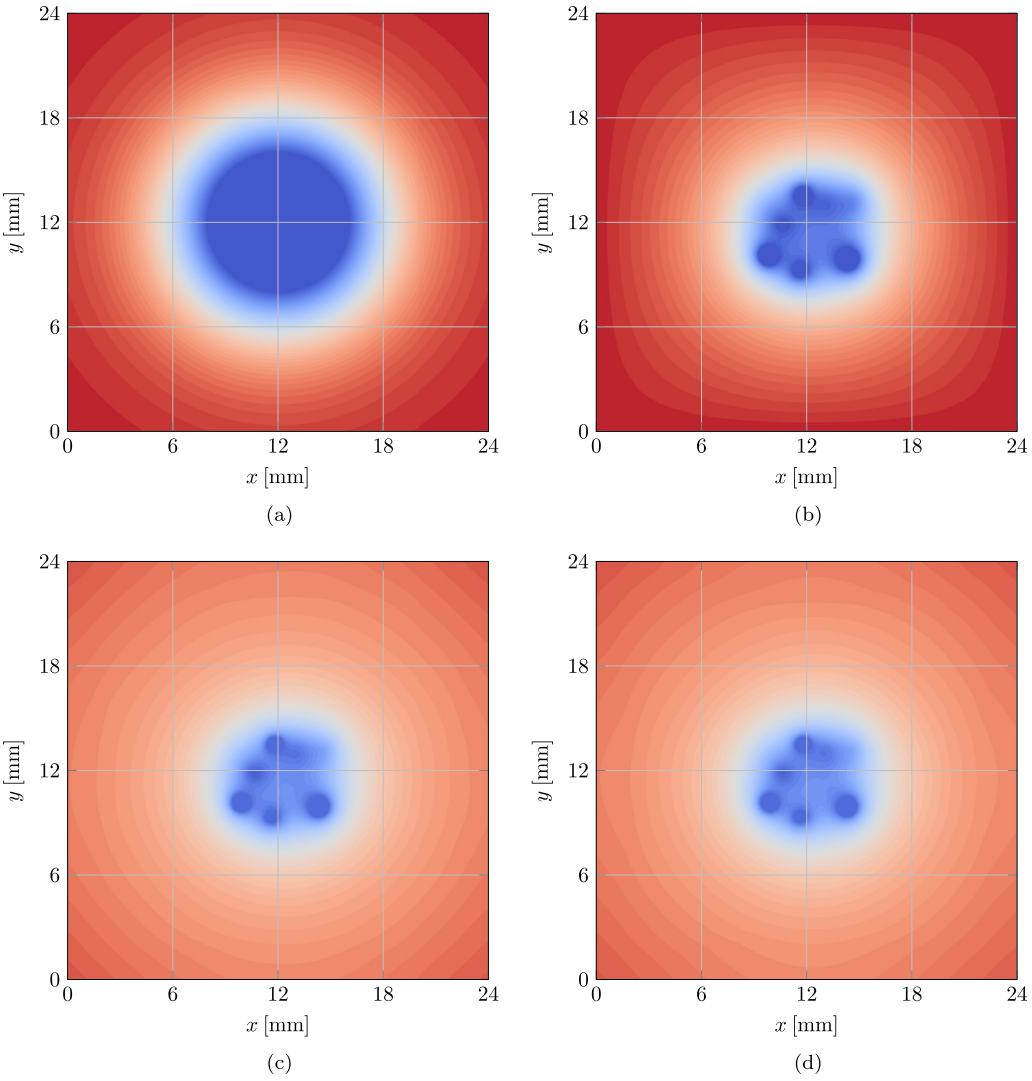

FIG. 22. Initial pressure field on a slice through the cloud center. (a) Simplification used in the paper at $t = 0$ μs, (b) solution of $\nabla^2 p = 0$ at $t = 0$ μs, (c) evolved pressure field at $t = 14$ μs with initial condition (a), and (d) evolved pressure field at $t = 14$ μs with initial condition (b). Blue corresponds to 0.1 MPa and red to 1.0 MPa.

fluctuating error of the evolving quantities $R_{\mathrm{B}_i}(t)$ and $p_{\mathrm{B}_i}(t)$ is measured by

$$L_2(y; t_s, t_e) = \sqrt{\frac{1}{t_e - t_s} \int_{t_s}^{t_e} \left| \frac{y - y_+}{y_+} \right|^2 dt}, \tag{A11}$$

where $y(t)$ is the subject function and $y_+(t)$ a reference associated with the fine grid G_+. We use a cubic spline interpolant to obtain a representation for y and approximate the integral in Eq. (A11) with a fourth-order Simpson quadrature. The data for the cubic spline interpolant is sampled at 2.53 MHz. Table V shows error measures based on Eq. (A11) evaluated for two time intervals $[0, t_{\mathrm{M},e}]$ and $[t_{\mathrm{M},e}, t_{\mathrm{C}}]$, which correspond to the interval of microjet analyses and region of peak pressure in the cloud, respectively. Values for $t_{\mathrm{M},e}$ are shown in Table III. The interval of the microjet

evluation $[t_{M,s}, t_{M,e}]$ and t_C are further highlighted in Fig. 21. The equivalent bubble radius R_{B_i} has converged in both regions of interest with a relative error of $2.8 \pm 0.9\%$ in the peak pressure region of the cloud, averaged over all bubbles. This is consistent with the error associated to the collapse period T_B reported above. The average bubble pressure p_{B_i} has similarly converged during the microjet evaluation interval with a relative error of $2.4 \pm 0.5\%$ averaged over all bubbles, while during the interval of peak pressure in the cloud the measured relative error is $13.2 \pm 5.8\%$. We note that the pressure averages discussed in Sec. III B propagate through both of these regions of interest and are associated with at most $13.2 \pm 5.8\%$ relative error during the final stage of the cloud collapse. This peak error is in the same order as the error measured for the microjet velocity magnitudes but occurs during the second interval of interest, while the error associated with the microjets occurs in the first interval. For the magnitude of the pointwise maximum pressure p_{peak}, reported in Sec. III A, we evaluate the local maximum measure $L_\infty(p_{B_i}; t_{M,e}, t_C) = 38.1 \pm 22.6\%$ on grid G_0, averaged over all bubbles. The large local error is mainly due to deviation in local pressure magnitude, not dislocation in time; see also Fig. 21(b). We report on the pointwise maximum pressure to orient the reader about its appearance in time; we do not elaborate on it further.

APPENDIX B: PRESSURE INITIAL CONDITION

This Appendix demonstrates the validity of the simplified pressure initial condition introduced in Sec. II C; see also Ref. [18]. For this assessment, we consider a small cloud with 10 bubbles at similar resolution as the production cloud presented in this paper. Figure 22 shows the initial pressure distribution on a slice through the cloud center for the simplified approach and an initial pressure field that satisfies the Laplace equation $\nabla^2 p = 0$ with Dirichlet boundary conditions at the bubble walls and domain boundaries. The initial pressure is 0.1 MPa inside the bubbles and 1.0 MPa in the far field. The problem is evolved using nonreflecting, characteristic-based boundary conditions [44–46] at the domain boundaries for both cases; see Sec. II C. Figure 22 further compares the pressure field after 14 μs corresponding to 2400 iterations. At this point, the simplified initial pressure has relaxed towards the Laplace reference with a relative error of $0.6 \pm 0.8\%$.

Figure 23 shows the evolution of the equivalent bubble radius R_{B_i} and the average bubble pressure p_{B_i}; see Eqs. (24) and (A10), respectively, for each of the 10 bubbles in the cloud. A slight delay in time is observed for the case of the simplified initial condition due to the initial pressure relaxation around the bubbles in the cloud. This process does not introduce artificial pressure oscillations. The

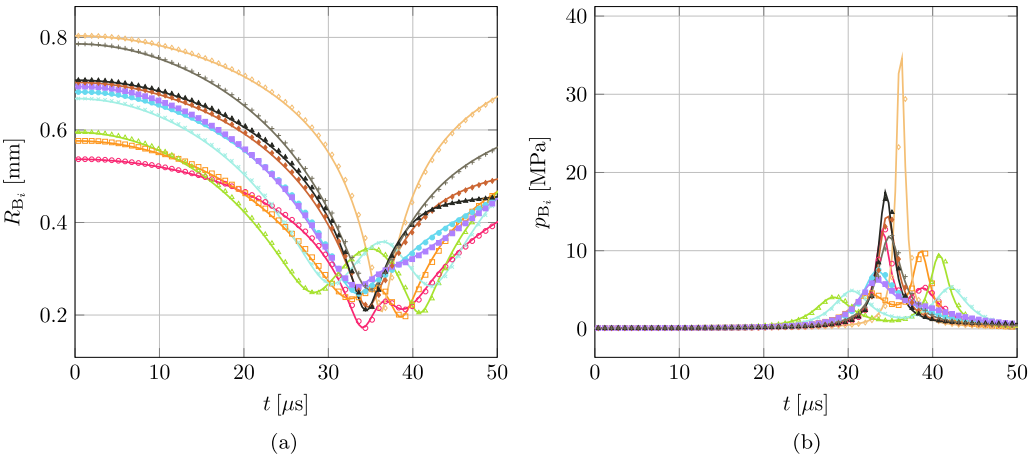

FIG. 23. Temporal evolution of individual bubbles. (a) Equivalent bubble radius R_{B_i} and (b) average bubble pressure p_{B_i} for bubble i. Solid lines correspond to the reference that initially satisfies $\nabla^2 p = 0$; symbols correspond to the solution obtained using the simplified initial pressure condition described in Sec. II C.

most important characteristics, such as time of minimum gas volume in the cloud, the individual time of minimum bubble volumes as well as time and magnitude of peak pressures are all preserved. This shows that the average and local features are not affected by the choice of a simplified initial pressure field, as its relaxation towards the pressure obtained for a field that initially satisfies the Laplacian takes place well before the fast scales of the cloud collapse appear. However, the induced relaxation time for the simplified case causes a very slight delay in the overall cloud collapse, but local bubble dynamics are not altered as shown by the temporal evolution of the bubble volume and average bubble pressure in Fig. 23. This confirms the validity of the simplified initial condition for the pressure field, originally introduced in Ref. [18]. A similar approximation has been verified for a single-bubble collapse in Ref. [31].

[1] X. Escaler, E. Egusquiza, M. Farhat, F. Avellan, and M. Coussirat, Detection of cavitation in hydraulic turbines, Mech. Syst. Signal Pr. **20**, 983 (2006).

[2] P. Kumar and R. Saini, Study of cavitation in hydro turbines—A review, Renew. Sust. Energ. Rev. **14**, 374 (2010).

[3] N. Mitroglou, V. Stamboliyski, I. Karathanassis, K. Nikas, and M. Gavaises, Cloud cavitation vortex shedding inside an injector nozzle, Exp. Therm. Fluid Sci. **84**, 179 (2017).

[4] T. Ikeda, S. Yoshizawa, M. Tosaki, J. S. Allen, S. Takagi, N. Ohta, T. Kitamura, and Y. Matsumoto, Cloud cavitation control for lithotripsy using high intensity focused ultrasound, Ultrasound Med. Biol. **32**, 1383 (2006).

[5] C. C. Coussios and R. Roy, Applications of acoustics and cavitation to noninvasive therapy and drug delivery, Annu. Rev. Fluid Mech. **40**, 395 (2008).

[6] Z. Xu, M. Raghavan, T. L. Hall, M.-A. Mycek, and J. B. Fowlkes, Evolution of bubble clouds induced by pulsed cavitational ultrasound therapy—Histotripsy, IEEE Trans. Ultrason. Ferroelectr. Freq. Control **55**, 1122 (2008).

[7] K. A. Mørch, On the collapse of cavity clusters in flow cavitation, in *Cavitation and Inhomogeneities in Underwater Acoustics*, edited by W. Lauterborn (Springer, Berlin, Heidelberg, 1980), pp. 95–100.

[8] G. E. Reisman, Y.-C. Wang, and C. E. Brennen, Observations of shock waves in cloud cavitation, J. Fluid Mech. **355**, 255 (1998).

[9] N. Bremond, M. Arora, C.-D. Ohl, and D. Lohse, Controlled Multibubble Surface Cavitation, Phys. Rev. Lett. **96**, 224501 (2006).

[10] E. Brujan, T. Ikeda, K. Yoshinaka, and Y. Matsumoto, The final stage of the collapse of a cloud of bubbles close to a rigid boundary, Ultrason. Sonochem. **18**, 59 (2011).

[11] K. Yamamoto, Investigation of bubble clouds in a cavitating jet, in *Mathematical Fluid Dynamics, Present and Future*, edited by Y. Shibata and Y. Suzuki (Springer, Tokyo, 2016), pp. 349–373.

[12] G. L. Chahine and R. Duraiswami, Dynamical interactions in a multi-bubble cloud, ASME J. Fluids Eng. **114**, 680 (1992).

[13] Y.-C. Wang and C. E. Brennen, Numerical computation of shock waves in a spherical cloud of cavitation bubbles, ASME J. Fluids Eng. **121**, 872 (1999).

[14] J. Ma, C.-T. Hsiao, and G. L. Chahine, Euler-Largange simulations of bubble cloud dynamics near a wall, ASME J. Fluids Eng. **137**, 041301 (2015).

[15] G. L. Chahine, C.-T. Hsiao, and R. Raju, Scaling of cavitation bubble cloud dynamics on propellers, in *Advanced Experimental and Numerical Techniques for Cavitation Erosion Prediction*, edited by K.-H. Kim, G. Chahine, J.-P. Franc, and A. Karimi, Fluid Mechanics and Its Applications Vol. 106 (Springer, Dordrecht, 2014), pp. 345–372.

[16] G. Peng, G. Tryggvason, and S. Shimizu, Two-dimensional direct numerical simulation of bubble cloud cavitation by front-tracking method, IOP Conf. Ser. Mater. Sci. Eng. **72**, 012001 (2015).

[17] N. A. Adams and S. J. Schmidt, Shocks in cavitation flows, in *Bubble Dynamics and Shock Waves*, edited by C. F. Delale, Shockwaves Vol. 8 (Springer, Berlin, Heidelberg, 2013), pp. 235–256.

[18] A. Tiwari, C. Pantano, and J. B. Freund, Growth-and-collapse dynamics of small bubble clusters near a wall, J. Fluid Mech. **775**, 1 (2015).
[19] J. Šukys, U. Rasthofer, F. Wermelinger, P. Hadjidoukas, and P. Koumoutsakos, Multilevel control variates for uncertainty quantification in simulations of cloud cavitation, SIAM J. Sci. Comput. **40**, B1361 (2018).
[20] R. P. Fedkiw, T. Aslam, B. Merriman, and S. Osher, A non-oscillatory Eulerian approach to interfaces in multimaterial flows (the ghost fluid method), J. Comput. Phys. **152**, 457 (1999).
[21] X. Y. Hu, N. A. Adams, and G. Iaccarino, On the HLLC Riemann solver for interface interaction in compressible multi-fluid flow, J. Comput. Phys. **228**, 6572 (2009).
[22] E. Lauer, X. Y. Hu, S. Hickel, and N. A. Adams, Numerical investigation of collapsing cavity arrays, Phys. Fluids **24**, 052104 (2012).
[23] L. Xu and T. Liu, Explicit interface treatments for compressible gas-liquid simulations, Comput. Fluids **153**, 34 (2017).
[24] G. Allaire, S. Clerc, and S. Kokh, A five-equation model for the simulation of interfaces between compressible fluids, J. Comput. Phys. **181**, 577 (2002).
[25] R. Saurel and R. Abgrall, A simple method for compressible multifluid flows, SIAM J. Sci. Comput. **21**, 1115 (1999).
[26] R. Saurel, F. Petitpas, and R. A. Berry, Simple and efficient relaxation methods for interfaces separating compressible fluids, cavitating flows and shocks in multiphase mixtures, J. Comput. Phys. **228**, 1678 (2009).
[27] A. Tiwari, J. B. Freund, and C. Pantano, A diffuse interface model with immiscibility preservation, J. Comput. Phys. **252**, 290 (2013).
[28] D. Rossinelli, B. Hejazialhosseini, P. Hadjidoukas, C. Bekas, A. Curioni, A. Bertsch, S. Futral, S. J. Schmidt, N. A. Adams, and P. Koumoutsakos, 11 PFLOP/s simulations of cloud cavitation collapse, in *Proceedings of the International Conference on High Performance Computing, Networking, Storage and Analysis, SC'13* (ACM, New York, 2013), pp. 1–13.
[29] P. E. Hadjidoukas, D. Rossinelli, F. Wermelinger, J. Šukys, U. Rasthofer, C. Conti, B. Hejazialhosseini, and P. Koumoutsakos, High throughput simulations of two-phase flows on Blue Gene/Q, in *Proceedings of the International Conference on Parallel Computing, Parallel Computing: On the Road to Exascale, ParCo 2015, 1–4 September 2015, Edinburgh, Scotland*, edited by G. R. Joubert, H. Leather, M. Parsons, F. Peters, and M. Sawyer (IOS Press, Netherlands, 2015), pp. 767–776.
[30] https://github.com/cselab/Cubism-MPCF.
[31] U. Rasthofer, F. Wermelinger, P. Hadjidoukas, and P. Koumoutsakos, Large scale simulation of cloud cavitation collapse, Procedia Comput. Sci. **108C**, 1763 (2017).
[32] M. R. Betney, B. Tully, N. A. Hawker, and Y. Ventikos, Computational modeling of the interaction of shock waves with multiple gas-filled bubbles in a liquid, Phys. Fluids **27**, 036101 (2015).
[33] A. Murrone and H. Guillard, A five equation reduced model for compressible two phase flow problems, J. Comput. Phys. **202**, 664 (2005).
[34] G. Perigaud and R. Saurel, A compressible flow model with capillary effects, J. Comput. Phys. **209**, 139 (2005).
[35] A. K. Kapila, R. Menikoff, J. B. Bdzil, S. F. Son, and D. S. Stewart, Two-phase modeling of deflagration-to-detonation transition in granular materials: Reduced equations, Phys. Fluids **13**, 3002 (2001).
[36] R. Menikoff and B. J. Plohr, The Riemann problem for fluid flow of real materials, Rev. Mod. Phys. **61**, 75 (1989).
[37] E. F. Toro, M. Spruce, and W. Speares, Restoration of the contact surface in the HLL-Riemann solver, Shock Waves **4**, 25 (1994).
[38] E. Johnsen and T. Colonius, Implementation of WENO schemes in compressible multicomponent flow problems, J. Comput. Phys. **219**, 715 (2006).
[39] V. Coralic and T. Colonius, Finite-volume WENO scheme for viscous compressible multicomponent flows, J. Comput. Phys. **274**, 95 (2014).
[40] G. S. Jiang and C. W. Shu, Efficient implementation of weighted ENO schemes, J. Comput. Phys. **126**, 202 (1996).

[41] S. Karni, Multicomponent flow calculations by a consistent primitive algorithm, J. Comput. Phys. **112**, 31 (1994).
[42] S. Gottlieb and C.-W. Shu, Total variation diminishing Runge-Kutta schemes, Math. Comput. **67**, 73 (1998).
[43] C. E. Brennen, Cloud cavitation: Observations, calculations and shock waves, Multiphase Sci. Tech. **10**, 303 (1998).
[44] K. W. Thompson, Time dependent boundary conditions for hyperbolic systems, J. Comput. Phys. **68**, 1 (1987)
[45] K. W. Thompson, Time dependent boundary conditions for hyperbolic systems II, J. Comput. Phys. **89**, 439 (1990).
[46] T. J. Poinsot and S. K. Lele, Boundary conditions for direct simulations of compressible viscous flows, J. Comput. Phys. **101**, 104 (1992).
[47] D. H. Rudy and J. C. Strikwerda, A non-reflecting outflow boundary condition for subsonic Navier-Stokes calculations, J. Comput. Phys. **36**, 55 (1980).
[48] L. d'Agostino and C. E. Brennen, Linearized dynamics of spherical bubble clouds, J. Fluid Mech. **199**, 155 (1989).
[49] C. E. Brennen, *Fundamentals of Multiphase Flow* (Cambridge University Press, Cambridge, 2005).
[50] H. Ganesh, S. A. Mäkiharju, and S. L. Ceccio, Bubbly shock propagation as a mechanism for sheet-to-cloud transition of partial cavities, J. Fluid Mech. **802**, 37 (2016).
[51] K. A. Mørch, On cavity cluster formation in a focused acoustic field, J. Fluid Mech. **201**, 57 (1989).
[52] L. van Wijngaarden, On the structure of shock waves in liquid-bubble mixtures, Appl. Sci. Res. **22**, 366 (1970).
[53] C. L. Merkle, J. Feng, and P. E. O. Buelow, Computational modeling of the dynamics of sheet cavitation, in *Proceedings of the Third International Symposium on Cavitation, Grenoble, France*, edited by J. M. Michel, H. Kato, and J. P. Franc (Universite Joseph Fourier, Grenoble, 1998), pp. 307–311.
[54] G. H. Schnerr, I. H. Sezal, and S. J. Schmidt, Numerical investigation of three-dimensional cloud cavitation with special emphasis on collapse induced shock dynamics, Phys. Fluids **20**, 040703 (2008).
[55] A. K. Singhal, M. M. Athavale, H. Y. Li, and Y. Jiang, Mathematical basis and validation of the full cavitation model, J. Fluids Eng. **124**, 617 (2002).
[56] I. Senocak and W. Shyy, A pressure-based method for turbulent cavitating flows, J. Comput. Phys. **176**, 363 (2002).
[57] C. Egerer, S. Hickel, and S. Schmidt, Large-eddy simulation of turbulent cavitating flow in a micro channel, Phys. Fluids **26**, 085102 (2014).
[58] R. F. Kunz, D. A. Boger, D. R. Stinebring, T. S. Chyczewski, J. W. Lindau, H. J. Gibeling, S. Venkateswaran, and T. R. Govindan, A preconditioned Navier-Stokes method for two-phase flows with application to cavitation prediction, Comput. Fluids **29**, 849 (2000).
[59] A. Jayaprakash, C.-T. Hsiao, and G. Chahine, Numerical and experimental study of the interaction of a spark-generated bubble and a vertical wall, ASME J. Fluids Eng. **134**, 031301 (2012).
[60] R. Mettin, I. Akhatov, U. Parlitz, C. D. Ohl, and W. Lauterborn, Bjerknes forces between small cavitation bubbles in a strong acoustic field, Phys. Rev. E **56**, 2924 (1997).
[61] I. A. Bolotnov, K. E. Jansen, D. A. Drew, A. A. Oberai, R. T. Lahey, and M. Z. Podowski, Detached direct numerical simulations of turbulent two-phase bubbly channel flow, Int. J. Multiph. Flow **37**, 647 (2011).
[62] J.-P. Franc and J.-M. Michel, *Fundamentals of Cavitation*, Fluid Mechanics and Its Applications, Vol. 76, 1st ed. (Springer, Netherlands, 2005).
[63] J. B. Keller and M. Miksis, Bubble oscillations of large amplitude, J. Acoust. Soc. Am. **68**, 628 (1980).
[64] K. Schmidmayer, S. H. Bryngelson, and T. Colonius, An assessment of multicomponent flow models and interface capturing schemes for spherical bubble dynamics, arXiv:1903.08242 [physics.flu-dyn].